ACS NANO

www.acsnano.org

Article

Nanomechanical Single-Cell Profiling Reveals Mechanical Dormancy Underlying Radiation Resistance in Polyploid Giant Cancer Cells

Minhee Ku,* Nara Yoon, Jin Sung Kim, Woong Sub Koom, and Jaemoon Yang*

Cite This: https://doi.org/10.1021/acsnano.6c04639

Read Online

ACCESS | Metrics & More | Article Recommendations | Supporting Information

ABSTRACT: Radiation therapy induces DNA damage primarily through reactive oxygen species, leading to cancer cell apoptosis. However, intratumoral heterogeneity and spatial dose variations often result in the survival of polyploid giant cancer cells (PGCCs), a therapy-resistant subpopulation characterized by multinucleation, genetic instability, and stem-like features. Particularly in malignant breast cancer, PGCCs contribute to recurrence by adopting a dormant yet invasive phenotype. Despite their clinical relevance, reliable tools to identify or characterize these cells remain lacking. Here, we present a nanomechanical single-cell profiling platform that enables high-resolution mechanomics of radiation-induced PGCCs. Through integrated cytoskeletal imaging and nanoscale stiffness mapping, we identify a distinct mechanical dormancy state, marked by cortical actin remodeling, nuclear enlargement, and biomechanical stiffening. This dormant mechanotype is coupled with suppressed proliferation yet sustained expression of invasion-associated markers, representing a latent therapeutic threat. Our findings position mechanical dormancy as a mechanobiological hallmark of radiation resistance and propose a predictive framework for optimizing radiotherapy thresholds. This platform enables mechanotype-guided stratification and precision-targeted intervention in radiation-refractory cancer.

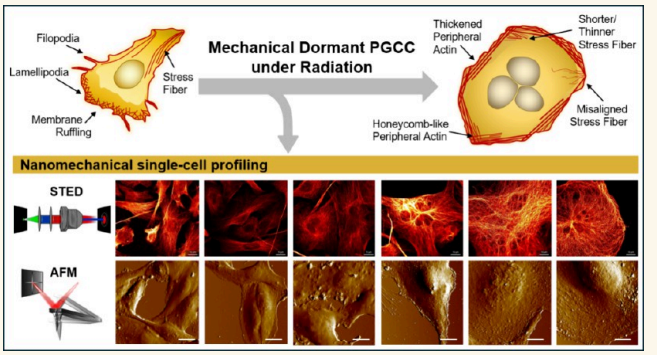

KEYWORDS: *nanomechanical, polyploidy giant cancer cell, mechanical dormancy, cortical stiffness, radiation therapy, single-cell profiling*

INTRODUCTION

Cancer cells undergo continuous selection, adaptation, and evolution in response to their microenvironment, enabling them to modify their phenotypes and survive under extreme conditions, including those imposed by cytotoxic agents such as chemotherapy and radiation. These treatments are designed to inhibit proliferation and induce cell death; however, paradoxically, they also exert selective pressure that allows a subset of cancer cells to persist and acquire therapy-resistant traits. Among these resistant populations, Polyploid Giant Cancer Cells (PGCCs) have garnered significant attention due to their ability to withstand lethal stress, evade apoptosis, and facilitate tumor recurrence and metastasis.[1,2] PGCCs emerge as a cellular response to radiation-induced DNA damage, resulting in aberrant mitotic events, polyploidization, and hypertrophy.[3] Especially, these enlarged, multinucleated cells have been closely associated with nanomechanical dynamics, aggressive cancer phenotypes, poor clinical prognosis, and metastatic potential.[1,4,5] While PGCCs were historically considered senescent or nonproliferative, accumulating evidence suggests that they serve as a reservoir for tumor regrowth through asymmetric division, giving rise to smaller, highly malignant progeny cells, often referred to as Raju cells.[6] These daughter cells exhibit enhanced metastatic capacity, therapy resistance, and the ability to initiate tumor relapse.[2,7,8] Despite their clinical relevance, the molecular and cellular mechanisms that enable PGCC-mediated therapeutic evasion remain poorly understood. While extensive research has been conducted on the biological characteristics of PGCCs, their mechanical properties remain largely unexplored. Given the critical role of mechanical cues in cellular behavior, it is imperative to evaluate mechanical dormancy in PGCCs and other therapy-resistant cancer cells.[9] Unlike highly migratory metastatic cells, which can be effectively targeted due to their distinct invasive behavior, dormant cancer cells pose a significant challenge in cancer treatment. These quiescent cells evade immune surveillance and standard therapies, remaining undetected for prolonged periods before reactivating to drive tumor progression. Therefore, establishing a single-cell mechanical profiling database that captures both shared and unique biomechanical properties of tumor cells is crucial

Received: March 12, 2026
Revised: April 2, 2026
Accepted: April 2, 2026

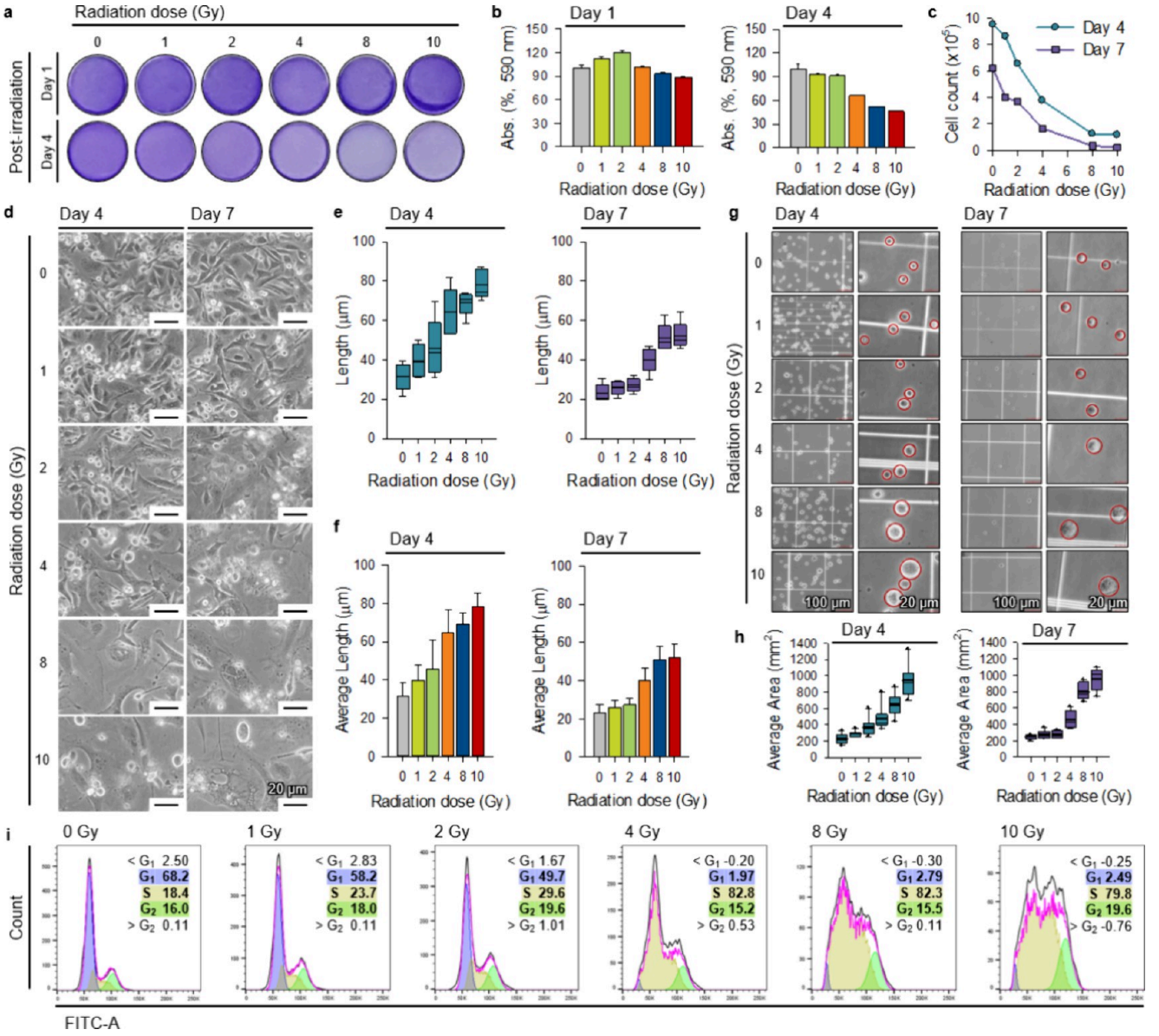

Figure 1. Dimensional characterization of radiation-induced giant cancer cells (PGCCs). MDA-MB-231 cells were subjected to X-ray doses of 0, 1, 2, 4, 8, and 10 Gy and subsequently cultured for 7 days. (a) Crystal violet staining images showing colony formation, and (b) quantification of crystal violet absorbance at day 1 and day 4 after irradiation (n = 4). (c) Cell viability graph of irradiated cancer cells at day 4 and day 7 postirradiation, determined by cell counts. (d) Phase-contrast microscopy images of irradiated cells showing morphological changes and PGCC formation at day 4 and day 7. Scale bars represent 20 μm. (e) Quantification of nuclear-to-cell boundary distance. (f) Average cell length measured from irradiated cells at day 4 and day 7 (n = 10). (g) Microscopy images of suspended cells detected using a hemocytometer (left, low magnification; right, high magnification). Red circles indicate suspended cells. Scale bars mean 100 and 20 μm. (h) Quantification of average cell area derived from panel g (n = 8). (i) Cell cycle distributions of irradiated cells determined by flow cytometry. Statistical significance was evaluated using one-way ANOVA followed by Tukey's multiple comparison test. Data are presented as mean ± SD (*p < 0.05, **p < 0.01, and ***p < 0.001).

for developing precision-targeted diagnostics and therapeutic strategies.

Single-cell biophysical analysis has emerged as a promising approach for assessing tumor heterogeneity and predicting therapeutic responses.[10−12] Recent findings suggest a strong correlation between cell surface stiffness, cytoskeletal organization, and metastatic potential, emphasizing the importance of mechanotyping in cancer research.[13] In particular, cortical stiffness plays a pivotal role in regulating cell motility, intracellular signaling, and treatment resistance, thereby influencing the effectiveness of radiation therapy.[14] However, due to the nanoscale dimensions of cytoskeletal components, including actin filaments (~7 nm), microtubules (~25 nm), and intermediate filaments (~10 nm), conventional imaging modalities lack the resolution required for detailed mechanobiological assessments.[15−19] To enable nanoscale mechanobiological analysis, we developed a nanomechanical single-cell profiling platform based on an integrated multicytoscopic analysis framework. This framework links quantitative readouts acquired from Atomic Force Microscopy (AFM), Confocal Microscopy, and Stimulated Emission Depletion (STED) Microscopy to achieve comprehensive, high-resolution characterization of PGCCs at the single-cell level. AFM provides topographical mapping and quantitative nanomechanical

https://doi.org/10.1021/acsnano.6c04639
ACS Nano XXXX, XXX, XXX−XXX

characterization of cell surface properties, while confocal and STED microscopy facilitate subcellular imaging of cytoskeletal architecture with super-resolution capabilities. Although individual actin monomers (~7 nm) remain below the effective resolution limit of STED microscopy, the Abberior STEDYCON platform used here provides a practical lateral resolution of ~30−40 nm, enabling clear visualization of higher-order actin network features such as filament bundling, continuity, and spatial heterogeneity.[20−22] Compared with confocal imaging, STED substantially reduces diffraction-induced blurring, allowing clearer delineation of cytoskeletal organization that is functionally relevant to cellular mechanics and invasive phenotypes. By integrating these cutting-edge imaging modalities, we established a nanotechnology-based single-cell mechanomics platform that enables precise profiling of PGCC-associated mechanotransduction, therapy resistance, and metastatic potential.

This study aims to investigate radiation-induced PGCC formation and its mechanobiological implications in triple-negative breast cancer (TNBC), a highly aggressive and heterogeneous cancer subtype characterized by poor treatment outcomes.[23,24] Given that TNBC lacks hormone receptors (ER, PR) and HER2 expression, patients rely heavily on conventional therapies, such as radiation, despite highly variable responses.[25] Reports indicate that discontinuing radiotherapy significantly increases recurrence risk, highlighting the urgent need for improved strategies to enhance radiation efficacy.[26] By integrating multicytoscopic analysis, our study seeks to elucidate the biomechanical alterations that drive radiation resistance in PGCCs. Furthermore, we investigate the role of MT1-MMP, an enzyme known to promote metastasis, in modulating actin dynamics and cortical stiffness within PGCCs. To validate our findings beyond cell-based models, we also employ an *in vivo* mouse xenograft model to investigate whether PGCC-associated mechanical and invasive phenotypes persist in the tumor microenvironment after radiation therapy. Leveraging advanced mechanotyping techniques, our work uncovers the interface between biological and mechanical dormancy in therapy-resistant cancer cells and provides a mechanistic foundation for developing personalized, mechanotype-guided interventions against radiation-refractory tumors.

RESULTS AND DISCUSSION

Radiation-Induced Cell Cycle Alterations Accompanied by Size Enlargement

To understand the biomechanical characteristics of PGCCs formed after radiation therapy, we planned an experiment to adjust the radiation doses for the TNBC MDA-MB-231 cells (Figure S1a). The objective is to investigate the correlation between radiation-induced morphological changes and alterations in nanomechanical properties by determining the radiation dose at which PGCCs begin to form and characterizing the cells under varying radiation conditions. Cancer cells were seeded in a 12-well plate and irradiated with radiation doses of 1, 2, 4, 8, and 10 Gy after 24 h. Radiation shielding collimators and lead were used to prevent interference between wells. First, cell viability after radiation exposure was confirmed using crystal violet (CV) staining (Figure 1a). As shown by the CV results, there was no critical change in cell viability on the first day after irradiation. However, by Day 4, a dose-dependent linear color change was observed in CV-stained cells, and the absorbance measured after solubilization treatment exhibited a similar trend (Figure 1b). Additionally, cell counting on Day 4 postirradiation showed a proportional decrease in cell number relative to the radiation dose (Figure 1c, circle). By Day 7, an even further reduction in cell count was observed (Figure 1c, rectangle). Morphological deformation on Day 4, coinciding with differences in cell viability, revealed the presence of PGCCs with abnormally enlarged cytoplasmic size, with significant morphological changes observed at 8 and 10 Gy (Figure 1d, left). These changes persisted and were further evident on Day 7 (Figure 1d, right). To further characterize morphological changes in detail, quantification of the nucleus-to-cell boundary distance and overall cell length demonstrated a progressive, dose-dependent increase following radiation exposure (Figure 1e, f). Significant radiation dose-dependent changes were observed on both Day 4 and Day 7, further confirming the impact of radiation on cellular morphology. Moreover, quantification of the diameter of individual single-cell clones in suspension revealed a significant increase at 8 and 10 Gy compared to other conditions on Day 4 (Figure 1g). To assess the persistence of radiation-induced morphological deformities, cells were monitored for up to 7 days postirradiation (Figure S1b). By Day 7, cells exposed to 1 and 2 Gy exhibited partial recovery in deformation rate relative to control cells (Figure 1h), whereas morphological deformities remained pronounced at 4, 8, and 10 Gy. Radiation exposure induces dose-dependent cell cycle alterations, with low doses (1−2 Gy) causing a reduction in the G1 population and an accumulation of cells in the S phase, indicative of checkpoint activation and DNA repair attempts (Figure 1i). At moderate doses (4 Gy), a substantial increase in S-phase arrest is observed, suggesting impaired DNA replication and a failure to transition into the G2 phase. High doses (8−10 Gy) further reinforce S-phase arrest, with a notable depletion of the G1 population and indications of polyploidy formation, likely contributing to radiation-induced cellular dormancy or mitotic catastrophe. These results confirm the existence of a threshold radiation dose that influences both cell viability and morphological deformation. It has been reported that the irregular and complex structural characteristics of cells reflect cellular heterogeneity, which is crucial for classifying cancer subtypes, analyzing drug responses, and monitoring cell cycle dynamics.[27] Additionally, our analysis revealed significant radiation-induced alterations in the cell cycle, including dose-dependent S-phase arrest and polyploidization, further supporting the impact of radiation on cellular behavior. Morphological deformation is closely linked to cytoskeletal organization, which governs the transmission of cyto-physical forces both intracellularly and extracellularly and plays a fundamental role in cellular mechanics.[28] Following radiation exposure, nuclear and cytoplasmic hypertrophy suggest that radiation-induced cytoskeletal modifications contribute to altered nanomechanical properties. Therefore, we aim to elucidate the correlation between radiation-induced cellular effects and mechanical properties through high-resolution cytoscopic analysis of cytoskeletal structural changes across different radiation doses.

Remodeling of Cytoskeletal Network in Radiation-Induced PGCCs

Cancer cells exhibit remarkable survival capabilities by acquiring resistance through alterations in their cytoskeletal network.[29,30] Modifications in cytoskeletal proteins are

https://doi.org/10.1021/acsnano.6c04639
ACS Nano XXXX, XXX, XXX−XXX

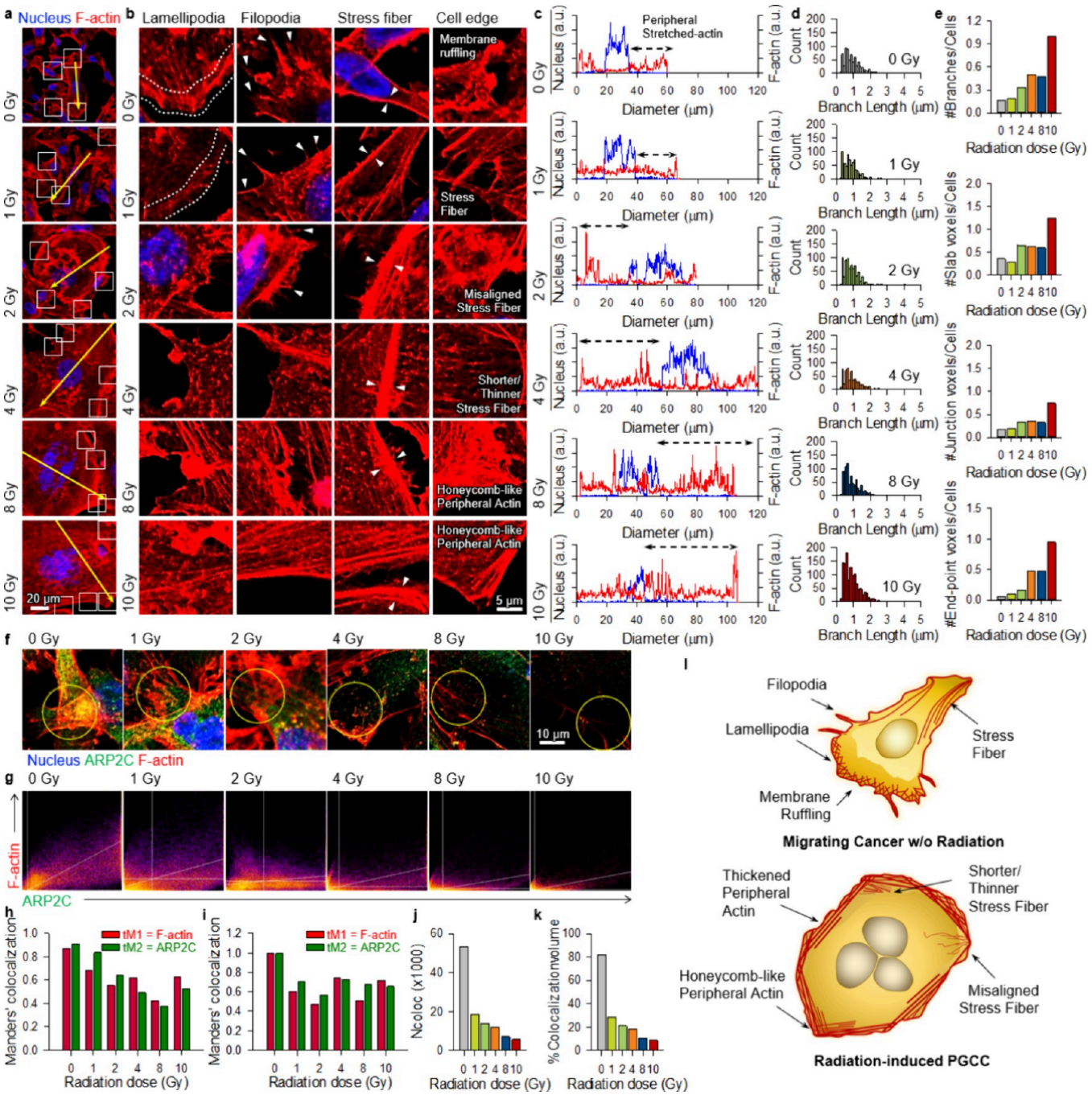

Figure 2. Cytoskeletal metrics analysis of F-actin organization and lamellipodia formation in radiation-induced PGCCs. (a) Confocal microscopy images of irradiated cancer cells stained with phalloidin (red). Nuclei are shown in blue. following X-ray irradiation. (b) Magnified confocal microscopy images of lamellipodia, filopodia, peripheral stress fibers, and cell edge region from the boxed areas indicate in panel a. Dotted lines indicate lamellipodia formation at the leading edge. White triangles mark actin structures in filopodia and variations in stress fiber thickness at the cell periphery. Text within the figure describes distinctive features of stress fiber structures at the cell edge. (c) Line profile analysis showing the intracellular distribution of the nucleus and F-actin fluorescence along the direction of the yellow arrows in (a). The left *y*-axis represents nuclear and the right *y*-axis represents F-actin fluorescence intensity. Dashed black arrows indicate peripheral stretched F-actin regions. (d) Histogram of F-actin branch lengths derived from skeletonization of confocal images. (e) Quantification of the counts of F-actin branches, slab, junctions, and end points pixels per cell, calculated using cytoskeletal network metrics (CNM). (f) Co-immunostaining of Arp2/3 complex subunit (ARP2C, green) and F-actin (red). Yellow circles denote the cell periphery regions where lamellipodia formation occurs. (g) Scatter plots were generated with linear regression lines and thresholds calculated by Manders' colocalization coefficients for channel 1 (red, *x*-axis) and channel 2 (green, *y*-axis). Bar graphs represent image-derived colocalization metrics from the representative images shown in f, comparing (h) the whole cell and (i) the cell periphery (ROI). (j) Graphs showing colocalization number (Ncoloc) and (k) %Colocalization volume calculated from panel (g). These values represent image-derived structural descriptors obtained from representative images and are presented descriptively rather than as population-averaged statistics. (l) Schematics illustration summarizing the mechanical deformation in radiation-induced PGCCs.

https://doi.org/10.1021/acsnano.6c04639
ACS Nano XXXX, XXX, XXX−XXX

particularly critical in the context of radiation therapy, as they can serve as predictive markers for cancer cell motility and invasiveness. To investigate the impact of radiation-induced cytoskeletal remodeling, we analyzed the distribution and morphological characteristics of filamentous actin (F-actin) in PGCCs formed following radiation exposure, using non-irradiated cells (0 Gy) as a control (Figure 2a) at a subcellular scale. Quantitative assessment of the cytoskeletal network, which is essential for maintaining cellular architecture, revealed a progressive increase in F-actin complexity across all radiation doses (Figure 2a). In the high-magnification images of the regions marked by white boxes in Figure 2a, distinct lamellipodia (white dashed lines) and filopodia (white triangles) are observed in nonirradiated cells (0 Gy), with prominent membrane ruffling at the cell periphery (Figure 2b). Here, the cell periphery was defined using a structure-based criterion rather than a fixed distance from the cell boundary. Specifically, the peripheral region corresponds to the nucleus-excluded outer cytoplasmic zone enriched with actin-dense leading-edge structures, including lamellipodia and filopodia, where F-actin and ARPC2 colocalize. Whole-cell boundaries were determined by F-actin–based segmentation. These cytoskeletal structures remain partially visible at doses up to 2 Gy; however, increasing disorganization and misalignment of actin fibers become evident. Exceeding 4 Gy, actin localization at the cell periphery is markedly altered, leading to the formation of thick stress fiber bundles, an increase in shorter and thinner stress fibers, and the emergence of honeycomb-like peripheral actin structures. Line profile analysis, indicated by yellow arrows in Figure 2a, demonstrates increasingly complex and intensified peaks of peripheral actin at the cell edges as radiation dose escalates (Figure 2c), highlighting the dose-dependent cytoskeletal reorganization induced by radiation exposure. Crucially, the analysis of nuclear size, polyploidy formation, and blue-fluorescent intensity changes, in conjunction with cell cycle data, confirmed the presence of giant cells and polyploidy in irradiated cancer cells.

On the other hand, image-based Cytoskeletal Network Metrics (CNM) analysis serves as a critical approach for evaluating the structural organization and network complexity of cytoskeletal components such as F-actin, which play a fundamental role in regulating cellular mechanics.[13] Based on pixel-based structural analysis of branched cytoskeletal networks, we thus observed a significant increase in Slab (with exactly two neighbors), Junction (with more than two neighbors), and End-point (with fewer than two neighbors) compared to a nonradiated control condition (Figure S2).[31] The heightened branching complexity within the cytoskeletal network suggests a diminished capacity of cells to establish stable and elongated actin filaments across the cytoplasm. Furthermore, branch length histograms demonstrated a shift toward shorter branches with increasing radiation dose, indicative of progressive cytoskeletal network fragmentation (Figure 2d). Remarkably, along with polyploidy formation and morphological enlargement, the complexity of the F-actin network exhibited a substantial increase, with a radiation dose-dependent rise in the number of branches per cell, as well as in Slab, Junction, and End-point pixels (Figure 2e). At radiation doses exceeding 4 Gy, the increase in cytoskeletal network complexity was accompanied by a critical reduction in cell height and enhanced cell spreading, as confirmed by orthogonal views, further reinforcing the structural alterations induced by radiation exposure (Figure S3). The cytoskeleton is a dynamic structure that extends throughout the cell and plays a fundamental role in cellular mechanics. In particular, cytoskeletal networks at the cell periphery assemble into diverse structures that regulate cell motility and function as key elements in this process.[32] Among these structures, lamellipodia, filopodia, and membrane ruffles are actin-driven protrusions that form at the leading edges of mesenchymal cells and are hallmarks of cell migration.[33] Given the inherently high motility of MDA-MB-231 cells, we hypothesized that radiation-induced disruption of cytoskeletal network connectivity would impair cell migration. To test this, we analyzed the distribution and structural organization of F-actin in individual cancer cell clones following radiation exposure.

Radiation-induced structural changes in the F-actin network, which directly influence cell shape deformation, suggest that cytoskeletal remodeling capacity may vary in its ability to maintain cellular morphology. To further explore the impact of cytoskeletal remodeling on cellular morphology, we analyzed the colocalization of ARPC (p34-Arc) and F-actin, both of which are essential for actin network formation and structural stability. ARPC2 is known to promote breast cancer cell growth and metastasis by regulating actin polymerization.[34] As a key actin-binding component of the ARP2/3 complex, ARPC2 plays a crucial role in nucleation-promoting factor (NPF)-mediated actin polymerization, facilitating the formation of branched actin networks.[35] The ARP2/3 complex, though lacking intrinsic enzymatic activity, facilitates actin polymerization by nucleating new filaments at a characteristic 70-degree branch angle upon activation by NPFs.[36,37] This process is essential for the formation of actin-driven protrusions, such as lamellipodia, and ARPC2-deficient cells exhibit diminished lamellipodia formation and significantly reduced migratory capacity compared to wild-type cells.[36] A radiation-induced reduction in ARPC2, which functions at actin branch junctions to regulate cytoskeletal integrity, leads to decreased F-actin dynamics and impaired actin remodeling capacity. Herein, we investigated the relationship between actin remodeling and lamellipodia formation by analyzing ARPC2 expression following radiation exposure. ARPC2 exhibited a gradual reduction across the entire cell area, accompanied by a significant decline in F-actin network integrity (Figure S4a). At 2 Gy, where ARPC2 expression remained detectable, protrusive structures were observed at the cell periphery (Figure 2f and Figure S4b). However, at radiation doses exceeding 4 Gy, ARPC2 expression was markedly reduced, and both the F-actin network within the cytoplasm and at the outer membrane exhibited signs of disintegration and degradation. These findings suggest that exceeding the critical radiation does significantly impairs actin remodeling, leading to a diminished capacity for lamellipodia formation and cytoskeletal reorganization in irradiated cells. Following radiation exposure, lamellipodia formation was assessed by identifying protrusive regions within the cellular periphery at the single-cell level, as indicated by yellow circles, and analyzing the colocalization of ARPC2 with F-actin (Figure 2f). Scatter plot analysis demonstrated complete colocalization with varying intensities under nonirradiated conditions, whereas partial colocalization was observed at 1 and 2 Gy (Figure 2g). Especially, at doses of 4 Gy and above, both fluorescence intensities decreased, and colocalization was significantly reduced, with minimal overlap between the two markers. Quantitative colocalization analysis further confirmed that colocalization coefficients (tM1 for F-actin and tM2 for

https://doi.org/10.1021/acsnano.6c04639
ACS Nano XXXX, XXX, XXX−XXX

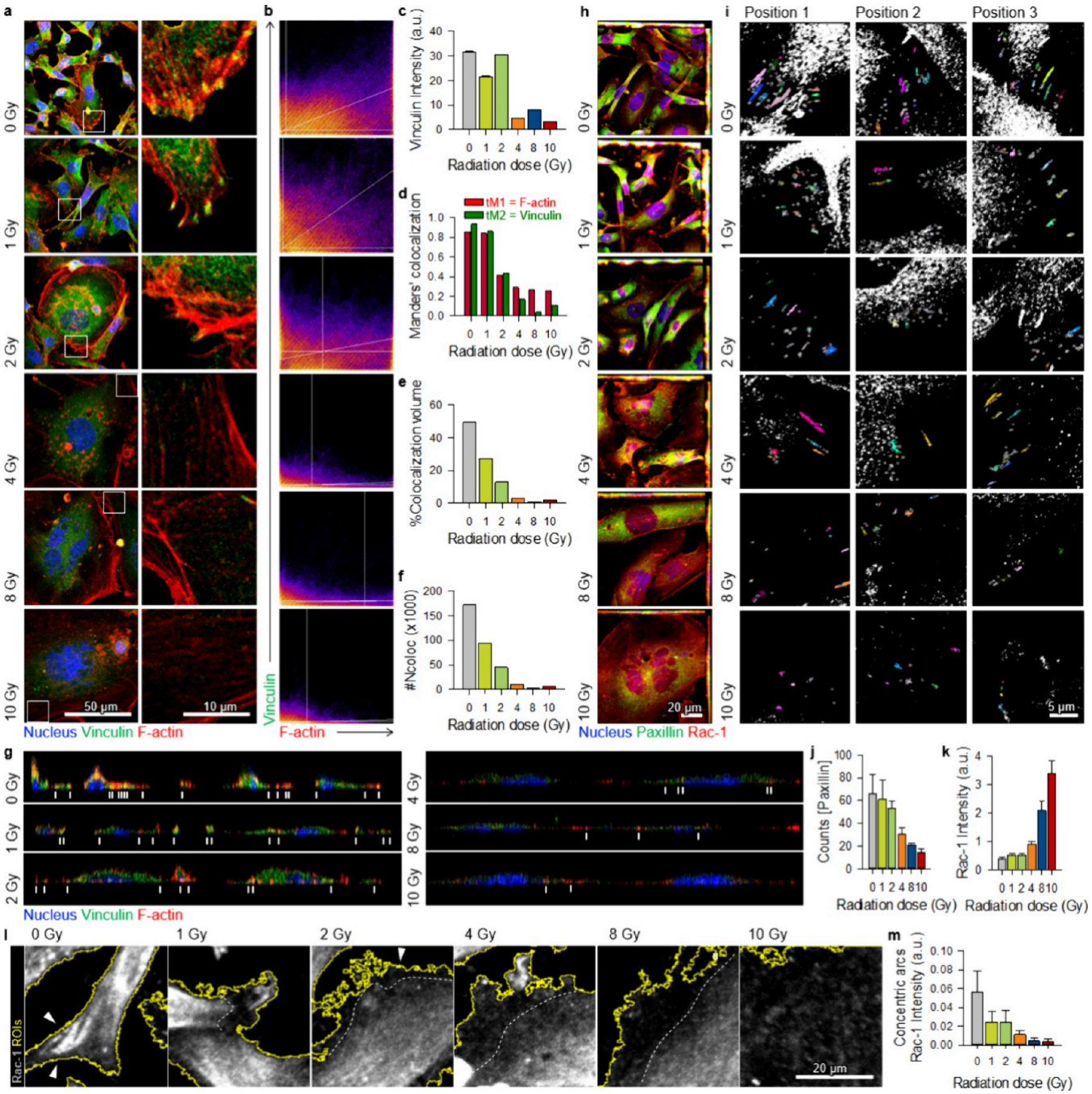

Figure 3. Destabilization of focal adhesions and loss of cell polarity in radiation-induced PGCCs. (a) Confocal microscopy images of irradiated cancer cells stained for Vinculin (green) and F-actin (red). Nuclei are shown in blue. White boxed regions indicate cell periphery areas displayed at higher magnification. Scale bars represent 50 μm (left) and 10 μm (right). (b) Pixel intensity scatter plots showing colocalization between F-actin (channel 1, red) and Vinculin (channel 2, green). (c) Quantification of Vinculin intensity derived from images in (a). (d) Manders' colocalization coefficients between F-actin and Vinculin. (e) Percentage colocalization volume and (f) colocalization number (Ncoloc) calculated from panel (a). (g) Lateral views of focal adhesion structures in irradiated cancer cells. White bars indicate focal adhesion sites along the cell membrane. (h) Intracellular distribution of Paxillin (green) and Rac-1 (red) observed via confocal microscopy. Nuclei are shown in blue. (i) Segmentation of Paxillin spots at three representative protrusion regions (positions 1−3). Scale bar represents 5 μm. (j) Quantification of Paxillin spot counts and (k) Rac-1 fluorescence intensity (n = 15). (l) Magnified images showing Rac-1 localization at lamellipodial concentric arc regions. (m) Quantification of Rac-1 signal intensity at lamellipodial concentric arcs. Data are presented as mean ± SD. Statistical comparisons were performed using one-way ANOVA followed by Tukey's multiple comparison test (*p < 0.05, **p < 0.01, and ***p < 0.001).

ARPC2), which reflect relative spatial overlap, progressively declined with increasing radiation dose (Figure 2h), a trend also observed at the cellular periphery (Figure 2i). Because Manders' coefficients do not necessarily scale linearly with absolute colocalization loss, we complemented this analysis with absolute metrics, including the colocalization count (Ncoloc, Figure 2j) and the percentage of colocalized volume (Figure 2k). Both metrics significantly decreased, consistently demonstrating a radiation dose-dependent reduction in lamellipodia formation. The cytoskeletal alterations observed

https://doi.org/10.1021/acsnano.6c04639
ACS Nano XXXX, XXX, XXX−XXX

at radiation doses of 4 Gy and higher exhibited patterns characteristic of F-actin network disruption, as illustrated in Figure 2l.[38,39] This disrupted actin architecture in PGCCs is also likely to influence focal adhesion formation. Thus, cytoskeletal rearrangement analysis of surviving cancer cells postradiation exposure revealed that PGCC formation was associated with an increase in cell area while lamellipodia formation was markedly reduced, impairing the ability to generate protrusive structures. These findings suggest that the transition from a mesenchymal-like cellular phenotype, characterized by cytoskeletal network remodeling, to PGCC morphology, may play a critical role in regulating and predicting cellular migratory capacity.

Radiation Impairs Focal Adhesion Formation in Radiation-Induced PGCCs

Focal adhesions (FAs), composed of multiprotein complexes, are formed through the binding of integrin-based adhesion complexes to the extracellular matrix (ECM) and their association with actin filaments at the leading edge of migrating cancer cells. These structures play a critical role in generating the tensile forces necessary for cell body retraction during migration.[40] As mechanosensitive structures, FAs dynamically regulate their assembly and disassembly in response to mechanical forces, forming a crucial link between the ECM and the cytoskeletal contractile machinery.[41] The ability of cancer cells to sense the external environment and adhere to the ECM is essential for cytoskeletal remodeling, mechanical stress adaptation, and signal transduction. Consequently, FA formation serves as a fundamental regulator of cell migration.[42] To investigate the correlation between radiation-induced mechanical changes in the cytoskeletal structure and focal adhesion (FA) complex formation, we conducted a colocalization analysis of core FA proteins, vinculin and F-actin, within the cell periphery (Figure 3a, first column). In the enlarged view of the cell periphery (Figure 3a, second column), distinct FA structures that were clearly visible under control progressively disappeared with increasing radiation dose. Furthermore, colocalization analysis revealed a reduction in yellow signal, representing FA clusters, suggesting a decline in vinculin and F-actin colocalization. This trend was further supported by a decreasing slope in the scatter plot (Figure 3b). The results demonstrated a marked reduction in vinculin expression across the entire cell area at radiation doses of 4 Gy or higher (Figure 3c). Manders' colocalization analysis was performed to quantitatively assess the spatial overlap between vinculin and F-actin.[43,44] Quantitative colocalization analysis demonstrated a dose-dependent decline in key parameters, including the threshold Manders' coefficient (tM1 for F-actin and tM2 for Vinculin, Figure 3d), the percentage of colocalization volume (Figure 3e), and the colocalization number (Ncoloc, Figure 3f), all of which indicate protein−protein overlap, independent of overall signal proportion. In orthogonal lateral views, focal adhesion complexes (indicated by white bars) were predominantly localized at the leading edge of the nucleus in control cells (Figure 3g). However, with increasing radiation doses, there was a progressive decrease in cell height and a reduction in the number of focal adhesions. These findings suggest that radiation-induced cytoskeletal disruption impairs focal adhesion formation and stability, ultimately leading to morphological alterations and potential functional deficiencies in cell adhesion and motility.

The interaction between radiation-induced mechanical alterations in cancer cells and the regulatory factors governing cytoskeletal structure and dynamics can be examined through FA formation, as indicated by vinculin and F-actin colocalization in protrusive structures (Figure 3). Vinculin enhances cell-to-cell and cell-to-matrix adhesions, linking the ECM to the cytoskeleton to regulate mechanical stability and FA formation, whereas paxillin plays a pivotal role in modulating cell motility by interacting with vinculin within FAs.[45,46] As a key component of integrin-mediated signaling, paxillin contributes to N-cadherin-based cell−cell adhesion and recruits focal adhesion kinase (FAK), facilitating the assembly of FA-like structures necessary for cell migration, division, and signal transduction.[47] Moreover, paxillin is implicated in down-regulating Rac-1 activity, thereby influencing cell spreading and adhesion stability.[48,49] Rac-1, a small GTPase of the Rho family, is integral to cell polarization, spreading, and cytoskeletal regulation, particularly through actin remodeling, lamellipodia extension, and membrane ruffling.[50−52] Elevated Rac-1 activity enhances cancer cell proliferation, migration, and metastatic potential, whereas its inactivation leads to the formation of actin-rich protrusions deficient in paxillin, resulting in impaired migratory capacity.[50] In especial, Rac-1 activity is spatially regulated: it undergoes activation upon translocation from the cytosol to the plasma membrane, promoting cell motility at the leading edge of lamellipodia. Conversely, cytoplasmic Rac-1 remains inactive, facilitating actin filament disassembly and altering cell morphology, thereby reducing migration potential.[51,53,54]

To investigate the relationship between cell shape remodeling and migratory capacity, we examined paxillin and cytosolic inactive Rac-1 expressions in protrusive structures of radiation-induced PGCCs. As shown in Figure 3h and Figure S5a, paxillin expression progressively decreased following X-ray irradiation. To further assess paxillin distribution in protrusive structures, which are critical for FA formation, adhesion sites were analyzed at three distinct positions within single cells (Figure S5b and Figure 3i). Quantitative analysis of paxillin spot area (Figure S6a) and spot counts (Figure 3j) revealed a significant reduction across all radiation conditions. Confocal microscopic imaging in 2.5D views demonstrated that paxillin expression declined with increasing radiation doses (Figure S6b), while cytosolic inactive Rac-1 intensity within single cells increased correspondingly (Figure 3k). Analysis of Rac-1 distribution along concentric arcs of the lamellipodium further confirmed a marked reduction in active Rac-1 localization at the protrusive edges (Figure S7 and Figure 3l). Consequently, despite the overall increase in cell spreading mediated by Rac-1 expression, the rise in inactive Rac-1 within the cytosol and its reduced localization in lamellipodia impaired paxillin-mediated adhesion stability (Figure 3m). This observation correlates with the loss of ARPC2-mediated actin organization (Figure 2f), aligning with the distinctive morphological characteristics of radiation-induced PGCCs. Collectively, the diminished paxillin expression and altered Rac-1 translocation in radiation-induced PGCCs suggest a direct association between the loss of protrusive structures and compromised cell migration ability. Given these findings, further investigation is warranted to explore additional structural changes affecting migration, as the observed disruption in FA formation and cytoskeletal remodeling are likely key contributors to the reduction in cellular motility after radiation exposure.

https://doi.org/10.1021/acsnano.6c04639
ACS Nano XXXX, XXX, XXX−XXX

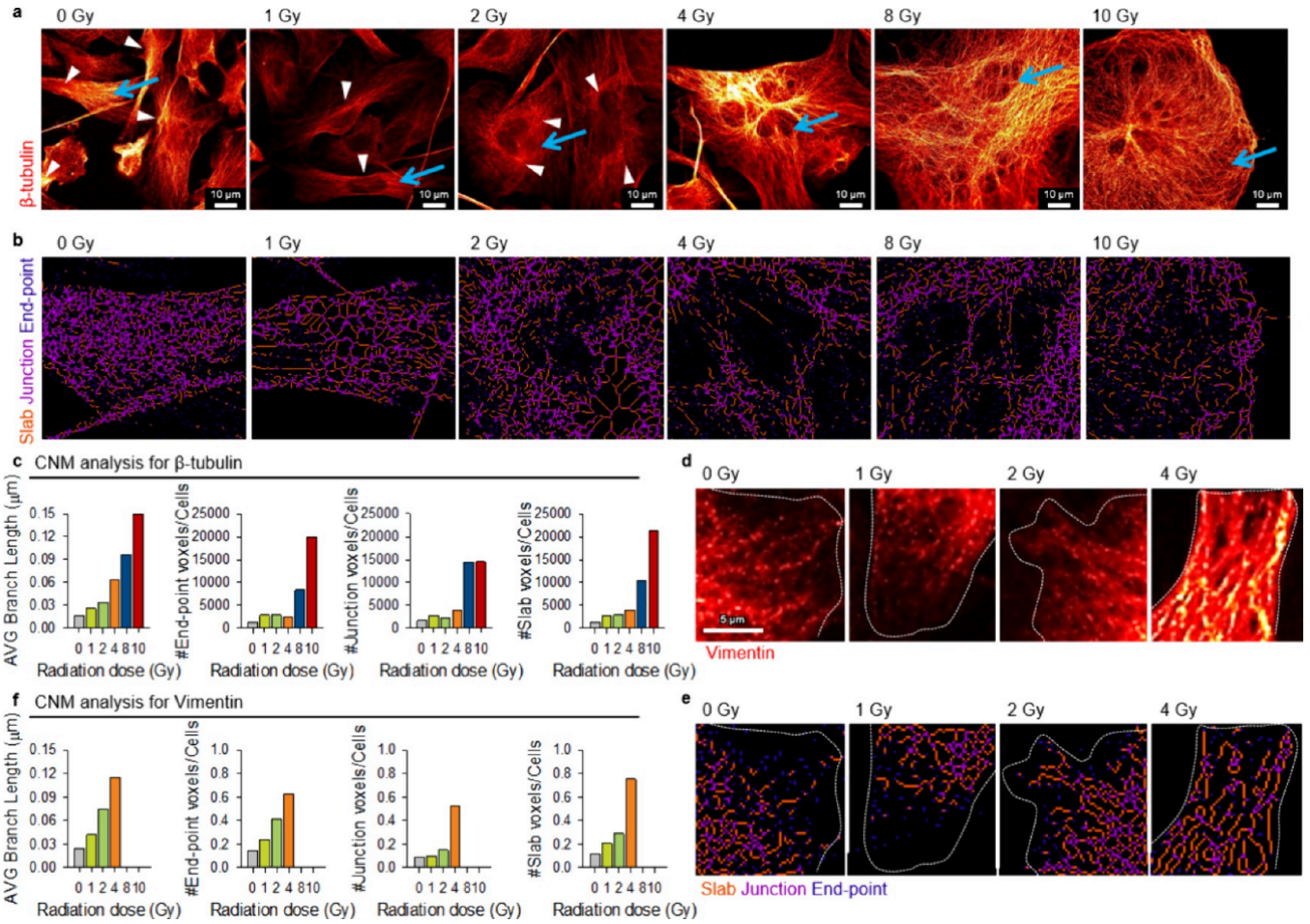

Figure 4. Dynamic variation of β-tubulin and Vimentin cytoskeletal architectures in radiation-induced PGCCs. (a) STED microscopy images presenting β-tubulin network in irradiated cancer cells. White triangles indicate microtubule-organizing centers (MTOCs). Scale bars represent 10 μm. (b) Image-based cytoskeletal network metrics (CNM) analysis of the β-tubulin network. Regions correspond to the locations indicated by sky-blue arrows in (a). (c) Quantitative CNM analysis of the β-tubulin network showing average branch length, end-points, junctions, and slabs derived from (b). (d) STED microscopy images presenting the Vimentin network in irradiated cancer cells. Scale bars represent 5 μm. (e) Image-based CNM analysis of the Vimentin network. (f) Quantitative CNM analysis of the Vimentin network showing average branch length, end-points, junctions, and slabs derived from (e).

Microtubule depolarization and vimentin redistribution impair directional stabilization in radiation-induced PGCCs

Other critical cytoskeletal components are tubulin and vimentin, which enhance mechanical resilience and facilitate epithelial-to-mesenchymal transition (EMT), a key process in cancer metastasis. In especial, vimentin supports cytoskeletal remodeling, cell polarity, and invasive potential, interacting with microtubules to stabilize cellular architecture.[55,56] Microtubules exhibit dynamic instability, alternating between growth, shortening, and regrowth, generating intracellular forces that regulate cell shape and mechanics through interactions with cytoskeletal components.[57,58] In migratory cells, microtubules direct the microtubule-organizing center (MTOC) toward the leading or trailing edge, playing a key role in cell polarity and migration.[59−61] To investigate these cytoskeletal dynamics, we employed Super-Resolution STED (Stimulated Emission Depletion) Microscopy for nanoscale imaging of vimentin and tubulin. Unlike conventional confocal microscopy, STED enables subdiffraction-limit resolution, providing detailed visualization of radiation-induced cytoskeletal remodeling and its impact on cancer cell migration and metastasis.[62,63]

To investigate metastatic motility, thus, super-resolution STED microscopy was employed to visualize the structural organization and distribution of β-tubulin and vimentin within irradiated cancer cells (Figure S8). As shown in Figure 4a, analysis of tubulin architecture revealed that up to 2 Gy, tubulin signals were enhanced and radiated from specific points near the nucleus in PGCCs. In particular, at doses exceeding 4 Gy, polyploidy became more pronounced, and the formation of giant cells was clearly observed. Furthermore, the microtubule network exhibited increased complexity, with an irregular distribution throughout the cytoplasm. To further investigate microtubule dynamics, Image-based CNM analysis following skeletonization provided deeper insights into centrosome displacement (Figure S9 and Figure 4b). Quantitative analysis of branch length and pixel-based parameters (number of end-points, junctions, and slabs per cell) confirmed a radiation dose-dependent increase in microtubule filamentation and structural complexity. Especially, the branch length of β-tubulin exhibited a progressive increase with rising radiation doses, accompanied by a corresponding elevation in other pixel-based parameters (Figure 4c). These findings indicate that radiation-induced

https://doi.org/10.1021/acsnano.6c04639
ACS Nano XXXX, XXX, XXX−XXX

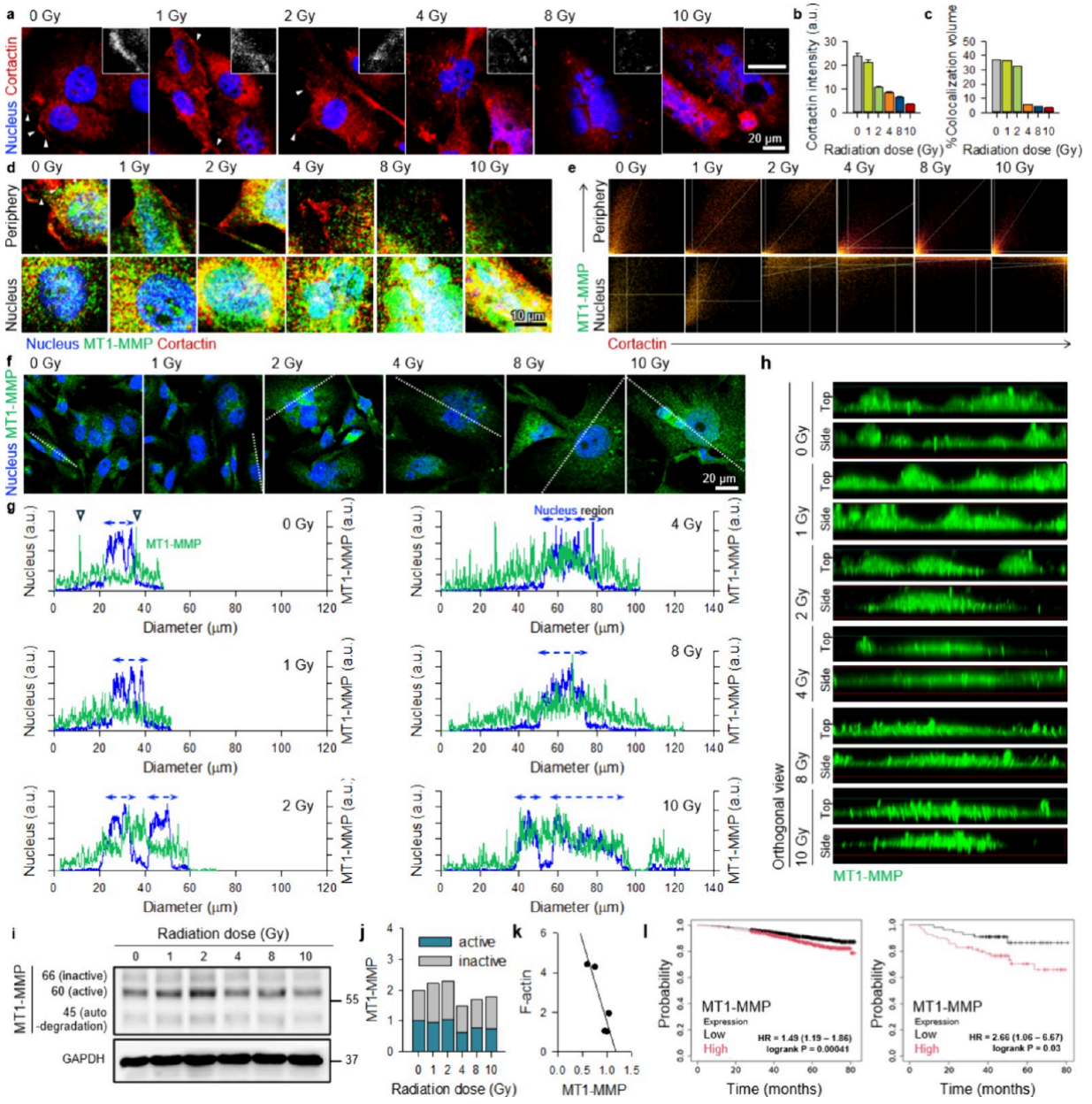

Figure 5. Cortactin-mediated recruitment of MT1-MMP related to the mechanics of radiation-induced PGCCs. (a) Confocal microscopy images showing Cortactin (red) translocation to the cell cortex regions in irradiated cancer cells. Nuclei are shown in blue. White triangles indicate cortical regions associated with membrane ruffles and lamellipodia. Insets show magnified views of the indicated regions. Scale bars represent 20 μm (main images) and 5 μm (insets). (b) Quantification of Cortactin intensity and (c) percentage colocalization volume derived from colocalization analysis between Cortactin and MT1-MMP in the membrane protrusion regions (n = 5). (d) Confocal microscopy images presenting MT1-MMP (green) and Cortactin (red) distribution in irradiated cancer cells. Upper panels show cell periphery regions and lower panels show nuclear regions. (e) Scatter plots of colocalization between Cortactin (channel 1, red) and MT1-MMP (channel 2, green) derived from images in (d). (f) Maximum intensity projection of MT1-MMP distribution obtained from confocal z-stack images. (g) Intensity line profiles of MT1-MMP (green) and Nuclei (blue) measured along the white dashed line in (f). Blue dashed double-headed arrows indicate nuclear region. (h) Orthogonal views of MT1-MMP distribution reconstructed from x/z (top) or y/z (side) planes. (i) Western blot analysis of MT1-MMP protein levels. (j) Quantification of MT1-MMP protein expression ratio between mature (enzyme and active, 60 kDa) and full-length latent (proenzyme and inactive, 63−66 kDa) forms. (k) Pearson correlation analysis between active MT1-MMP expression and F-actin network complexity. (l) Kaplan−Meier survival plots analyzing overall survival based on MMP14 (MT1-MMP) expression in all breast cancer (left) and TNBC (right) patients, derived from publicly available data sets. Data are presented as mean ± SD. Statistical comparisons were performed using one-way ANOVA followed by Tukey's multiple comparison test (*p < 0.05, **p < 0.01, and ***p < 0.001).

alterations in microtubule dynamics contribute to a loss of cell polarity, resulting in a more static cellular state with impaired migratory potential. The increased microtubule network complexity and irregular filamentation suggest a shift from a highly organized cytoskeletal arrangement, which supports cell motility, to a disordered state, limiting directional movement. To further substantiate these observations, quantitative polarity analysis could be conducted by assessing the spatial distribution of the centrosome relative to the nucleus and examining MTOC reorientation (Figure 4a, white triangles)

https://doi.org/10.1021/acsnano.6c04639
ACS Nano XXXX, XXX, XXX−XXX

under varying radiation doses. Additionally, integrating STED imaging of microtubule dynamics could provide direct evidence of reduced cytoskeletal adaptability, confirming the functional consequences of radiation-induced cytoskeletal reorganization on cellular movement and mechanical stability.

On the other hand, vimentin expression was predominantly observed in cells exposed to 0−4 Gy, where network analysis of the entire image area revealed reduced perinuclear clustering and the formation of irregularly branched structures throughout the cytoplasm (Figure S8). However, at radiation doses of 8 Gy or higher, vimentin intensity diminished dramatically, indicating a disruption in cytoskeletal integrity. The organization of vimentin within the lamellipodia region is closely associated with cell motility. In motile cells, vimentin typically extends across the rear and perinuclear regions, whereas in the lamellipodia, it primarily exists as nonfilamentous vimentin particles. In contrast, in serum-starved or nonmotile cells, vimentin tends to extend across the entire cell periphery.[64] As shown in Figure 4d, vimentin extended to the cell periphery at 4 Gy, a condition where lamellipodia formation was impaired. Conversely, in control conditions, where cells exhibited high motility, vimentin networks in the lamellipodia region appeared as particle-like structures. To further characterize radiation-induced vimentin remodeling, STED-based CNM analysis was employed. Branch length, number of end-points, junction pixels, and slab pixels per cell were quantified, demonstrating a progressive increase in vimentin network complexity with increasing radiation dose (Figure 4e, Figure S10). Notably, branch length exhibited a significant increase, accompanied by a dose-dependent elevation in pixel-based metrics, confirming a greater degree of cytoskeletal complexity (Figure 4f). These findings provide quantitative evidence that radiation-induced vimentin remodeling contributes to directionality instability in irradiated cancer cells. Ultimately, STED-based CNM analysis of β-tubulin and vimentin revealed that PGCCs exposed to high radiation doses undergo a loss of cell polarity and reduced cell motility, further supporting the hypothesis that cytoskeletal disorganization underlies radiation-induced mechanical dormancy. Mechanical dormancy refers to a nonproliferative cellular state in which cancer cells maintain structural integrity and exhibit increased stiffness, allowing them to survive therapeutic stress while remaining temporarily inactive.

Radiation-Induced Alteration in Proinvasiveness of PGCCs

We investigated the correlation between radiation-induced nanomechanical changes and cell migration potential by analyzing key structural and functional markers following X-ray exposure. To determine whether mechanical properties at the single-cell level correlate with invasive behavior, we examined the localization of cortactin and actin-rich puncta, which indicate mature invadopodia formation, a critical feature of cancer cell invasion.[65] Cortactin, a cytoskeletal remodeling protein, shuttles between the cytoplasm and nucleus and is translocated to the cell cortex in response to actin polymerization and increased cell motility.[66] In highly invasive cells, cortactin localizes to membrane protrusions, contributing to a promigratory phenotype.[67,68] Its translocation to lamellipodia and membrane ruffles aligns with active cytoskeletal reorganization and invadopodia maturation.[69] Considering the significance of cortactin's subcellular localization, we analyzed its distribution at the single-cell level (Figure 5a). In nonirradiated control cells (0 Gy), cortactin was predominantly localized within protrusions, and even at 1−2 Gy, partial retention of cortactin within filopodia was observed. However, at radiation doses above 4 Gy, cortactin was increasingly localized to the cytoplasm and nucleus, accompanied by a reduction in overall intensity (Figure 5b). At 8 and 10 Gy, cortactin was nearly absent from membrane ruffles and lamellipodia, indicating a disruption in cytoskeletal organization. Cortactin plays a key regulatory role in ECM degradation rather than directly influencing invadopodia formation.[70] It does not significantly alter the expression levels of invadopodia-associated proteases, including matrix metalloproteinases (MMPs), ARP2, β-actin, or invadopodia size.[65] Instead, cortactin facilitates the targeted delivery and secretion of MMP-2 and MMP-9, while also regulating MT1-MMP (MMP14) surface expression.[65,71] Furthermore, cortactin colocalizes with Arp2/3 to drive actin polymerization, supporting the recruitment of MT1-MMP at sites of ECM degradation.[72] Invadopodia formation progresses in distinct stages, beginning with actin and cortactin accumulation at cell-ECM attachment sites, which marks the initiation phase. In the preinvadopodia stage, MT1-MMP expression increases, alongside a rise in actin and cortactin levels. The transition to mature invadopodia is characterized by intensified actin polymerization and MT1-MMP recruitment, ultimately leading to ECM degradation.

To further evaluate FA stability and invasive potential, we analyzed the colocalization of cortactin and MT1-MMP in the protrusive regions of the cell periphery (Figure S11). With increasing radiation dose, the expression levels of both cortactin and MT1-MMP decreased compared to non-irradiated control cells. A dose-dependent reduction in colocalization volume (%) was also confirmed at radiation doses of 4 Gy and above (Figure 5c). Furthermore, a comparative analysis of cortactin and MT1-MMP localization in the nuclear and peripheral regions revealed distinct distribution patterns. Specifically, in cellular membrane protrusions, cortactin expression decreased, accompanied by a reduction in colocalization with MT1-MMP (Figure 5d). In contrast, a marked increase in MT1-MMP intensity was observed around the nucleus following radiation exposure (Figure 5e). These results highlight the significance of MT1-MMP localization in determining its functional role, suggesting that its redistribution from the periphery to the nuclear region may contribute to the altered invasive capacity of irradiated cancer cells.

Subsequently, we examined fluorescence localization and protein expressions to validate MT1-MMP function. Since MT1-MMP levels increase within the nucleus at higher radiation doses, global intensity-based analysis was insufficient for quantifying MT1-MMP activity. To address this, we performed line profiling at the single-cell level (white dashed line, Figure 5f). Under nonirradiated conditions, MT1-MMP intensity was highest in the cell periphery compared to the nucleus region (blue dashed double-headed arrows) (Figure 5g). However, from 4 Gy onward, MT1-MMP intensity near the nucleus increased, while peripheral MT1-MMP expression progressively declined with increasing radiation doses (Figure 5h). Western blot analysis revealed an overall reduction in total MT1-MMP protein expression following 4 Gy or higher radiation doses, with a notable decrease in the enzymatically active 60 kDa form of MT1-MMP (Figure 5i,j). These results suggest that radiation-induced PGCC formation leads to a decrease in cortactin-MT1-MMP colocalization at FA sites,

https://doi.org/10.1021/acsnano.6c04639
ACS Nano XXXX, XXX, XXX−XXX

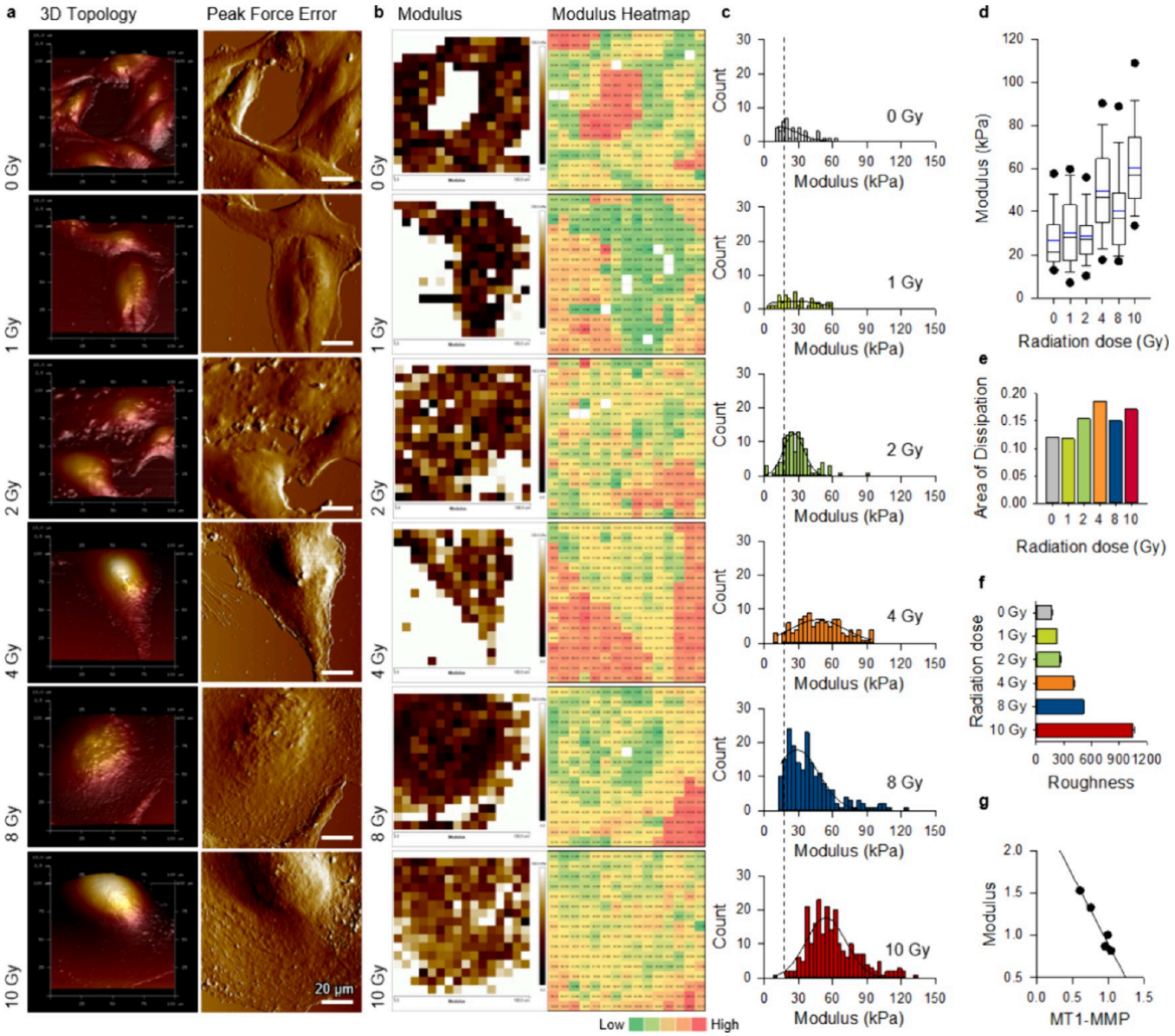

Figure 6. AFM-based nanomechanical single-cell profiling of radiation-induced PGCCs. (a) Atomic force microscopy (AFM) images of irradiated cancer cells acquired in PeakForce quantitative nanomechanical mapping (PeakForce QNM) mode, depicting 3D topography (left) and peak force error (right). Scale bar represents 20 μm. (b) Modulus map obtained using force-volume (FV) mode. Left panels display pixelized modulus maps, and right panels illustrate color-coded modulus heat maps. (c) Histograms representing the distribution of cortical modulus values in irradiated cancer cells. The dashed line indicates the maximum modulus value observed in control cells (0 Gy). (d) Box plots of the distribution of cellular modulus values (kPa) across radiation doses (n = 30). Statistical comparisons were performed using the Kruskal–Wallis test followed by Dunn's multiple comparison test (***p < 0.001). (e) Quantification of energy dissipation area derived from FV mode measurements. (f) Average 3D surface roughness (Sa) extracted from pixelized AFM height images. (g) Pearson correlation analysis evaluating the relationship between active MT1-MMP expression and cellular modulus. Modulus values were obtained from single-cell AFM measurements.

impairing actin polymerization and ECM remodeling. This aligns with our prior findings, where a decline in MT1-MMP expression correlated with increased cell modulus and decreased motility, reinforcing the connection between radiation exposure and mechanical dormancy.[13] To further explore the clinical implications of MT1-MMP reduction, we performed Pearson correlation analysis between F-actin network complexity and MT1-MMP activity (Figure 5k). The results demonstrated strong correlations (R^2 > 0.9), highlighting the structural-functional relationship underlying radiation-induced changes in cancer cells.

To provide clinical context for the biological relevance of MT1-MMP, we analyzed publicly available breast cancer data sets to assess the association between MMP14 expression and overall survival. Kaplan–Meier survival analysis revealed that breast cancer patients with high MMP14 expression exhibited a 1.49-fold higher relative risk of mortality (HR = 1.49, 95% CI: 1.19–1.86), with a highly significant log-rank p-value of 0.00041 (Figure 5l).[73] In TNBC, patients with high MMP14 expression had a 2.66-fold higher relative risk of death compared to those with low expression (HR = 2.66, 95% CI: 1.06–6.67), with a log-rank p-value of 0.03, demonstrating a statistically significant impact on survival outcomes. These

https://doi.org/10.1021/acsnano.6c04639
ACS Nano XXXX, XXX, XXX–XXX

analyses are based on public data sets and are intended to contextualize the potential clinical relevance of MT1-MMP, rather than to establish a direct prognostic claim within the scope of the present study. Through integrative multicytoscopic analysis, we revealed that MT1-MMP plays a pivotal role in regulating the interaction between morphological deformation and metastatic potential following radiation exposure. The correlation between active MT1-MMP expression and F-actin network complexity suggests that incorporating these markers into mechanical profiling could enhance the predictive accuracy of cancer cell behavior postradiation therapy. These insights emphasize the importance of targeting MT1-MMP-mediated cytoskeletal remodeling in developing therapeutic strategies for radiation-resistant metastatic cancer cells.

Radiation Increases Both Cortical Stiffness and Membrane Perturbation of PGCCs

The relationship between cytoskeletal network remodeling and mechanical stiffness following radiation exposure provides critical insights into the metastatic potential of cancer cells. Understanding how alterations in cytoskeletal integrity influence cortical stiffness can offer valuable predictive markers for assessing cancer cell invasiveness under X-ray radiation. In particular, cancer cells generally exhibit lower stiffness compared to normal cells, a characteristic observed across multiple cancer types.[74,75] In fact, studies have demonstrated that as few as 100 soft cancer cells can effectively form tumors in immune-regulated mice, whereas their stiffer counterparts show reduced tumorigenic potential.[76] The flexibility and decreased elasticity of cancer cells allow them to navigate through narrow anatomical spaces, facilitating metastasis through circulation and tissue invasion. This nanomechanical distinction highlights the significance of cell stiffness as a marker for tumor progression and metastatic capacity.

Since cytoskeletal networks play a central role in defining cell morphology and cortical stiffness, we employed AFM to investigate the correlation between morphological changes and nanomechanical alterations in PGCCs. To quantify cortical stiffness, we utilized a BioScope Resolve AFM in PeakForce Quantitative Nanomechanical (QNM) mode, which simultaneously captures mechanical properties and surface topology at high spatial resolution (Figure 6a). Peak force error images provided enhanced visualization of fine surface details that are often difficult to discern in height images due to the large depth range, commonly referred to as the deflection error signal. This signal, obtained by subtracting the set-point force from the actual deflection, highlights feature edges, making it particularly useful for imaging soft materials like cancer cells.[77,78] Given that large error signals can hinder precise tip−sample interactions, PeakForce QNM mode proved to be the optimal technique for examining the surface characteristics of cancer cells.

To assess whether the observed single-cell mechanical changes after radiation exposure correlate with alterations in cell stiffness, we conducted a comparative analysis of nanomechanical properties at the individual cell level. Given the complexity of cellular structures composed of various organelles, we mapped overall mechanical properties rather than focusing on specific subcellular locations. Cellular modulus was measured using Force-Volume (FV) mode, which generates force−displacement curves at each pixel (Figure 6b, left). Although FV mode operates slower than QNM mode, it provides precise nanoscale mapping of cell height, stiffness, and energy dissipation.[79−81] Modulus map plots acquired from pixelated cell surfaces (16 × 16 pixels) were reconstructed into heat maps, where stiff substrates appeared red, and softer regions displayed green to yellow gradients (Figure 6b, right). At 0 and 1 Gy, cancer cells exhibited a green distribution, whereas at 2 Gy and above, yellow regions became more prominent, indicating increased stiffness. A remarkable transition was observed at doses exceeding 4 Gy, indicating a potential shift toward mechanical dormancy (Kruskal−Wallis test, $p < 0.001$). To enhance monitoring accuracy, a histogram of modulus values revealed a rightward shift of the peak at 4, 8, and 10 Gy, corresponding to radiation-induced mechanical changes (Figure 6c). The black dashed lines drawn from the 0 Gy histogram peak further illustrate this shift, emphasizing the increasing rigidity of PGCCs. Moreover, the box plot of elastic modulus values confirmed a significant increase in modulus beyond 4 Gy, as indicated by rising median (black lines) and mean values (blue lines) (Figure 6d).

Another crucial parameter for characterizing cellular mechanical heterogeneity at the nanoscale is energy dissipation.[82] AFM allows for precise analysis of surface roughness and mechanical responses through phase imaging, which captures the interactions between the AFM tip and the sample surface. Energy dissipation is primarily linked to the frequency shift of the AFM cantilever, particularly when oscillated at its resonance frequency. Under conditions of high-intensity pulsed electric fields, increased cell surface roughness, membrane damage, and cytoskeletal disruption contribute to higher energy dissipation values.[83,84] Thus, energy dissipation mapping provided a comprehensive characterization of the mechanical properties of irradiated cancer cells (Figure S12a). Elevated dissipation signals corresponded to increased energy loss at the cell surface, indicative of enhanced surface roughness, molecular scattering, and cytoskeletal irregularities. In parallel, as radiation dose increased, the distribution width of energy dissipation expanded, reflecting a progressive rise in mechanical heterogeneity among individual cells (Figure S12b, Figure 6e). This observation suggests that radiation-induced mechanical alterations contribute to cellular mechanical dormancy, a state characterized by reduced proliferation and motility.

Cytoskeletal network analysis further demonstrated that radiation doses exceeding 4 Gy led to a critical decrease in the height of both the nucleus and cytoplasm (Figure S13a,b). This observation, supported by actin distribution patterns and lateral cell morphology, suggests that actin filament remodeling within the cortical region significantly contributes to increased cell rigidity. To further investigate the impact of radiation on cellular surface roughness, we quantitatively analyzed nuclear region roughness at the single-cell level. In regulated cell death (RCD) pathways such as apoptosis, necrosis, and ferroptosis, nanoscale membrane perturbations, including blebbing and pore formation, are associated with increased roughness.[85] By designating the interfacial region above the nucleus (Figure S13b, yellow rectangle), we compared surface roughness (Sz) based on maximum height using an image color scale (Figure S13c). At 2 Gy, the roughness histogram showed a rightward shift compared to nonirradiated controls. However, at radiation doses exceeding 4 Gy, a leftward shift was observed, indicating a reduction in z-axis height within the cortical region (Figure S13c,d). Additionally, analysis of key surface profile

https://doi.org/10.1021/acsnano.6c04639
ACS Nano XXXX, XXX, XXX−XXX

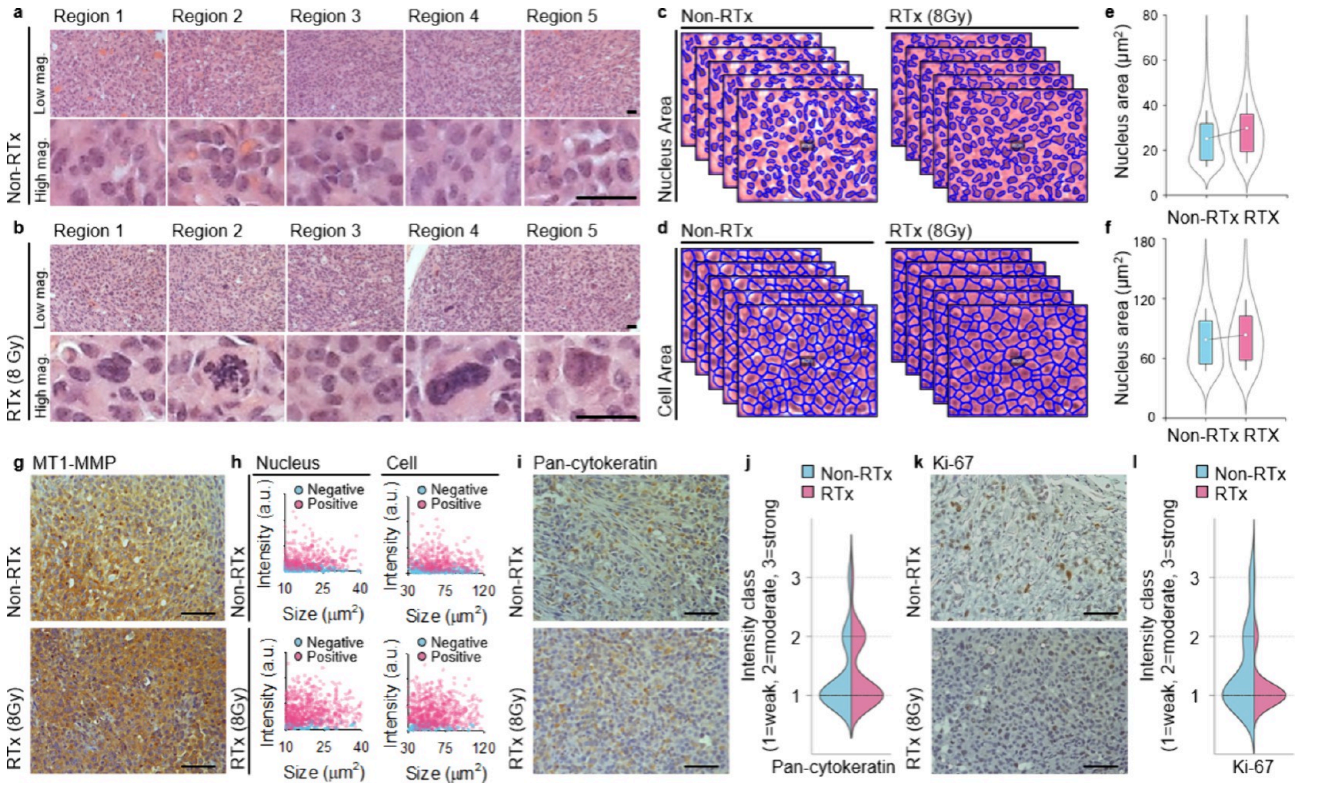

Figure 7. Radiation-induced PGCC formation and phenotypic remodeling in Xenografts. Hematoxylin and eosin (H&E)-stained tumor sections from nonirradiated (a, Non-RTx) and irradiated (b, RTx, 8 Gy) mice. Enlarged nuclei and cytoplasmic expansion characteristic of PGCC morphology are observed in RTx tumors. Five representative tumor regions were analyzed for each condition. Scale bars represent 50 and 25 μm. Segmentation maps derived from histological images illustrating (c) nuclear area and (d) cell area distributions in Non-RTx and RTx tumors. Violin plots depicting the distribution of (e) nuclear area and (f) cytoplasmic area between Non-RTx and RTx tumors. (g) Immunohistochemical staining of MT1-MMP in tumor tissues. Scale bars represent 50 μm. (h) Colored scatter plots evaluating the relationship between MT1-MMP intensity and nuclear or cell size. (i) Immunohistochemical staining of Pan-cytokeratin, indicating partial disruption of epithelial structural organization in RTx tumors. Scale bars represent 50 μm. (j) Split violin plot quantifying Pan-cytokeratin intensity classes. (k) Immunohistochemical staining of K_i-67, demonstrating reduced nuclear positivity in RTx tumors. Scale bars represent 50 μm. (l) Split violin plot quantifying K_i-67 intensity classes.

parameters, including Sq (root-mean-square roughness, Figure S13e), Sa (3D surface roughness average, Figure 6f), and Smax (maximum peak-to-valley difference, Figure S13f), demonstrated a significant increase in cortical roughness. The measured membrane perturbation indicated that radiated cancer cells undergo RCD processes with increasing radiation doses. To further explore the relationship between mechanical changes and cancer cell behavior, we conducted a Pearson correlation analysis between nanomechanical properties (modulus) and the activity of the metastasis-associated protein MT1-MMP (Figure 6g). Here, modulus values were strongly correlated with MT1-MMP expressions ($R^2 > 0.9$), indicating that suppression of MT1-MMP–mediated proteolytic activity is associated with increased cortical stiffness.

Our results demonstrate that nanomechanical analysis provides a powerful framework for understanding the impact of radiation on cytoskeletal remodeling, mechanical stiffness, and metastatic potential. The integration of energy dissipation and surface roughness analysis reveals critical alterations in cellular mechanics following radiation exposure. Moreover, disruption of the actin cytoskeleton significantly influences cancer cell survival, reinforcing the strong correlation between physical properties and cellular fate.[86,87] Furthermore, the mechanical stiffness of PGCCs serves as a key biomarker for identifying treatment-resistant cancer cells and predicting RCD processes following therapy. This study highlights the potential of nanomechanical analysis as a label-free diagnostic tool for cancer prognosis and treatment evaluation. Future research should focus on developing advanced mechanical profiling techniques to elucidate further the mechanistic links among cytoskeletal integrity, metastatic behavior, and therapeutic resistance in cancer cells.

Nanomechanical Profiling Reveals Radiation-Induced Mechanical Dormancy and Invasive Persistence of PGCCs

To evaluate whether PGCC phenotype and mechanical dormancy observed *in vitro* also manifest *in vivo*, we established MDA-MB-231 xenograft models by subcutaneously injecting tumor cells into immunocompromised mice. Upon tumor establishment, animals were subjected to localized X-ray irradiation at 8 Gy, and the resulting tumor tissues were analyzed in comparison with nonirradiated controls (Non-RTx). H&E staining revealed distinct morphological differences between the two groups (Figure 7a, b). In irradiated tumors, enlarged nuclei and giant cell phenotypes characteristic of PGCCs were consistently observed across multiple regions (high magnification), mirroring the cellular features previously identified *in vitro*. To quantitatively assess nuclear and cytoplasmic alterations, sophisticated segmentation analysis was performed (Figure 7c,d). Nuclear and cytosolic area segmentation revealed an overall increase in nuclear and cell

https://doi.org/10.1021/acsnano.6c04639
ACS Nano XXXX, XXX, XXX−XXX

size following irradiation. Violin plot analysis (Figure 7e,f) further substantiated these findings, demonstrating that the mean nuclear size increased from 25.0 μm^2 in Non-RTx tumors to 29.7 μm^2 in RTx tumors, while the mean cell size increased from 78.4 μm^2 to 83.8 μm^2, respectively. These results confirm that radiation induces significant morphological reprogramming in tumor cells *in vivo*, consistent with the emergence of PGCCs.

To assess whether these structural changes were associated with altered invasive potential, we examined MT1-MMP expression, a membrane-anchored metalloproteinase critical for ECM degradation. Immunohistochemistry revealed elevated MT1-MMP levels in RTx tumors (Figure 7g), and single-cell intensity mapping demonstrated a positive correlation between increased MT1-MMP expression and nuclear or cell size (Figure 7h), suggesting that PGCCs may maintain or enhance their proteolytic capacity. We further analyzed the expression patterns of Pan-cytokeratin, an epithelial structural marker, and K_i-67, a proliferation marker, to characterize radiation-induced phenotypic remodeling *in vivo* (Figure 7i,k). Representative immunohistochemistry images illustrate a modest redistribution of Pan-cytokeratin staining intensity and a marked reduction in K_i-67 positivity in tumors exposed to 8 Gy irradiation. Quantitative analysis using split violin plots (Figure 7j,l) stratified staining into three ordinal classes, weak (1+), moderate (2+), and strong (3+), revealed distinct shifts in expression patterns (Table S1). For Pan-cytokeratin, the RTx group exhibited a rightward redistribution toward higher intensity classes, with an increased proportion of moderate (2+, 7.10%) and slightly decreased strong (3+, 0.98%) staining compared to Non-RTx controls (2+, 6.05%; 3+, 1.88%). These data suggest attenuation of epithelial cytoskeletal architecture following radiation exposure. In addition, K_i-67 staining intensity sharply declined postradiation, with RTx tumors exhibiting a greater fraction of weakly stained cells (1+, 14.10%) and a dramatic loss of moderate (2+, 1.76%) and strong (3+, 0.29%) signals compared to Non-RTx tumors (1+, 9.52%; 2+, 3.33%; 3+, 1.43%), indicating suppressed proliferative activity. H-score values further confirmed these changes, decreasing from 38.98 to 32.93 for Pan-cytokeratin and from 20.48 to 18.50 for K_i-67 upon irradiation. The overall proportion of positively stained cells remained similar or slightly reduced after radiation, with a shift toward weaker expression levels, particularly for K_i-67. Given that K_i-67 is expressed in all active phases of the cell cycle but absent in G0, this redistribution suggests that a significant fraction of tumor cells entered a quiescent or cell cycle−arrested state following irradiation. Such growth arrest may result from checkpoint activation in response to DNA damage, leading to senescence, apoptosis, or mechanical dormancy. Taken together, these findings indicate that X-ray radiation induces substantial phenotypic remodeling in tumor cells *in vivo*, characterized by redistribution of epithelial cytoskeletal markers (Pan-cytokeratin) and marked suppression of proliferative activity, as reflected by reduced K_i-67 positivity. Rather than representing a simple loss of epithelial identity, these changes are consistent with cytoskeletal reorganization and the emergence of a mechanically dormant state. This mechanically dormant phenotype, associated with cellular hypertrophy, cytoskeletal remodeling, and proliferative arrest, likely represents an adaptive survival state of residual tumor cells following radiation exposure. Importantly, despite this proliferative suppression, MT1-MMP expression, a key mediator of extracellular matrix degradation, remains sustained or elevated, suggesting that invasive competence is preserved. This coexistence of proliferative dormancy and invasion-associated signaling highlights a potentially critical mechanism by which radiation-surviving PGCCs evade cytotoxic stress while retaining the capacity to contribute to tumor recurrence or metastatic dissemination. Collectively, these observations support the hypothesis that radiation can drive a mechanotype transition toward mechanical dormancy, underscoring the value of integrating cytomechanical and molecular profiling to evaluate post-therapy tumor states.

Mechanical Dormancy of Radiation-Induced PGCCs Revealed through Cyto-Mechanomics

To further elucidate the relationship between nanomechanical changes and metastatic potential following radiation exposure, we conducted a Cyto-Mechanotype Distance Matrix (CMDM) analysis. This analytical method categorizes cellular data based on the similarity of expression patterns, enabling the identification of clusters that reveal intricate interrelationships among cellular characteristics. By employing CMDM analysis, we aimed to visually represent the correlation between radiation-induced cellular changes obtained through multi-cytoscopic analysis. Importantly, the CMDM approach serves as an analytical framework designed to assess whether quantitative single-cell−level metrics acquired across distinct spatial resolutions converge in describing a common biological state. The radiation-induced mechanical phenotypic changes observed in this study are not stochastic events confined to individual cells, but reproducible and conserved responses that emerge under defined experimental conditions. These characteristics justify the use of a multimodal analytical approach based on condition-matched independent sample sets.

We thus classified Cyto-Mechanotypes into 13 categories, encompassing various cellular properties, including morphological deformity (Figure 1e), cytoskeletal network instability (Figure 2e), lamellipodia formation (Figure 2k), focal adhesion formation (Figure 3e), cell polarity disruption (Figure 3j), focal adhesion stabilization (Figure 3k), microtubule depolarization (Figure 4c), directional stabilization (Figure 4f), metastatic migration factor (Figure 5b), mature invadopodia formation (Figure 5c), proinvasive factor (Figure 5j), cortical stiffness (Figure 6d), and membrane perturbation (Figure 6f),.

The CMDM heatmap illustrated that greater proximity to red indicated higher dissimilarity in expression patterns between cellular variables, while the main diagonal was rendered in white (Figure S14a). In particular, cortical stiffness exhibited the highest nonlinear correlation with mature invadopodia formation, characterized by the colocalization of MT1-MMP and cortactin at the cell periphery. Conversely, the most pronounced linear correlation was identified with cytoskeletal network instability. These results demonstrate that cortical stiffness is linearly associated with cellular morphological alterations but nonlinearly correlated with parameters reflecting cell motility and directionality. This distinction was further confirmed by logarithmic ratio fluctuations between cortical stiffness and other cellular variables in response to radiation dose (Figure S14b). These insights indicate a complex interplay between cortical stiffness and key cellular processes, emphasizing the intricate nano-mechanical responses to radiation exposure. The proposed CMDM approach proved highly effective in quantitatively

https://doi.org/10.1021/acsnano.6c04639
ACS Nano XXXX, XXX, XXX−XXX

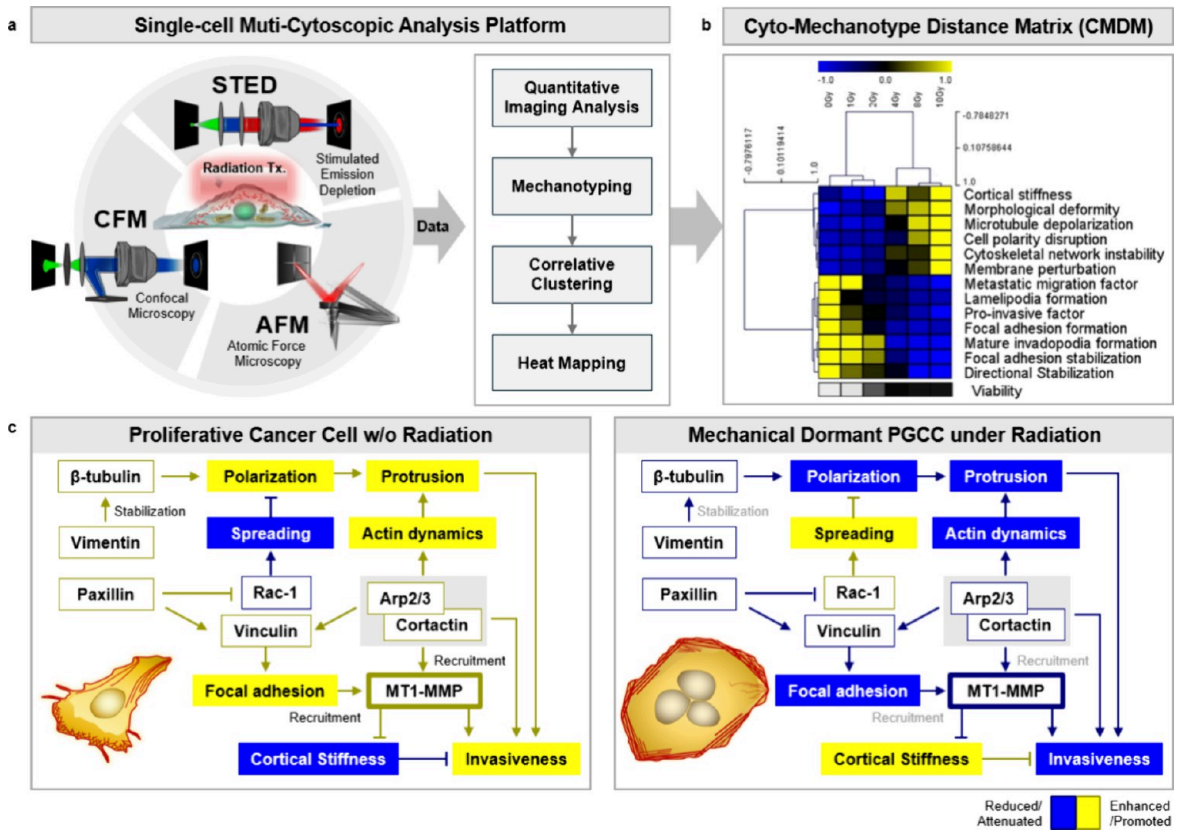

Figure 8. Integrated cytoscopic analysis framework for mechanomics of radiation-induced PGCCs. (a) Schematic overview of the single-cell multicytoscopic analysis framework combining AFM, CFM, and STED microscopy. Nanomechanical, morphological, and cytoskeletal features are independently acquired under identical experimental conditions and subsequently analyzed through quantitative imaging and mechanotyping, correlation clustering, and heat-map visualization. (b) Cyto-Mechanotype Distance Matrix (CMDM) derived from multiparameter feature analysis. Hierarchical clustering heatmaps illustrate similarity relationships among cortical stiffness, morphological deformity, cytoskeletal network organization, and various mechanotransductive factors associated with cell viability. (c) Schematic of cytoskeletal regulation and mechanotransduction in proliferative cancer cells without radiation (left) and mechanically dormant PGCCs induced by radiation (right). This schematic illustrates the regulatory interactions linking cortical stiffness to key cellular processes, including cell polarity disruption and microtubule depolarization, and highlights the importance of their interactions in determining cell migration potential.

comparing diverse radiation-induced cellular changes and mapping their interrelationships. Particularly, this method can capture nonlinear interactions, offering a deeper understanding of how cellular cortical stiffness influences a broad spectrum of biological functions. Through this approach, we systematically analyzed critical nanomechanical attributes, such as radiation-induced cytoskeletal remodeling, cell motility, and adhesion stability, ultimately providing valuable insights for evaluating and predicting the efficacy of radiation therapy. CMDM analysis is anticipated to serve as a vital tool in understanding the intricate biophysical alterations occurring in cancer cells postradiation exposure.

Our study further underscores the necessity of investigating single-cell mechanical properties within the context of cancer therapy. By analyzing cytoskeletal network organization, polymerization dynamics, actin cross-linker interactions, and cortical stiffness in PGCCs, we identified key biophysical traits that define their metastatic behavior. Moreover, we established a strong correlation between cytoskeletal integrity and the expression of metastasis-promoting enzymes, suggesting that single-cell analysis could serve as a powerful tool for predicting cancer cell dissemination (Figure 8a).

To enable these insights, we implemented an integrative multicytoscopic approach, combining AFM and STED microscopy, providing a high-resolution platform for examining complex cellular structures and molecular interactions. This innovative strategy allowed us to precisely assess single-cell mechanical properties and predict the threshold radiation doses required for effective therapy. The hierarchical diagram in Figure 8b systematically illustrates the effects of radiation therapy on various cellular functions, offering a comprehensive perspective on the interplay between nanomechanical alterations and metastatic characteristics.

The results demonstrate that radiation exposure induces profound cytoskeletal remodeling, affecting key structural proteins such as actin, tubulin, and vimentin. Notably, these alterations were accompanied by a reduction in cell polarization and protrusion formation, impairing migratory ability. Additionally, the progressive decline in MT1-MMP activity and the increase in cortical stiffness indicated a transition into mechanical dormancy (Figure 8c). Herein, our results suggest that radiation-induced environmental stress triggers a state of mechanical dormancy, enabling cancer cells to survive in a metastasis-suppressed state. However, despite this adaptive response, the potential for reactivation remains a significant threat, underscoring the need for precise characterization of these biophysical states for effective targeted therapy and drug discovery. Considering these findings, future research should focus on the relationship between tumor stiffness, stromal mechanics, and immune evasion mechanisms. By targeting

https://doi.org/10.1021/acsnano.6c04639
ACS Nano XXXX, XXX, XXX−XXX

mechanotransduction pathways related to cellular stiffness, it may be possible to enhance immune responses and improve therapeutic efficacy. This approach offers a systemic strategy to maximize treatment outcomes while minimizing adverse effects, leveraging both the biophysical and molecular characteristics of cancer cells for precision medicine.

CONCLUSIONS

Our study establishes nanomechanical single-cell profiling as a preclinical mechanomics strategy for elucidating fundamental mechanisms underlying therapy resistance in cancer. Using an integrated cytoscopic analysis framework, we identified distinct mechanophenotypic signatures that distinguish metastatic migration from mechanical dormancy, a radiation-induced adaptive state characteristic of polyploid giant cancer cells (PGCCs). This mechanical dormancy phenotype is defined by cytoskeletal stiffening, reduced proliferative activity, and sustained invasion-associated molecular reprogramming. These transitions were closely associated with MT1-MMP activity and cortical actin remodeling. Importantly, consistent mechanotype shifts were observed across both *in vitro* systems and *in vivo* xenograft models, where radiation exposure induced PGCC formation, cytoskeletal reorganization, and persistent expression of invasion-related markers. Within this analytical framework, AFM-based nanomechanical profiling quantitatively captures the physical outcomes of these phenotypic adaptations, confocal microscopy resolves global cellular morphology and focal adhesion–associated structural remodeling, and STED microscopy provides nanoscale insight into the cytoskeletal architecture underlying these alterations.

Quantitative features derived from these complementary modalities are brought into a shared analytical space within the Cyto-Mechanotype Distance Matrix (CMDM) framework, and their relationships are evaluated through correlation and multivariate analyses. This approach demonstrates mechano-phenotypic convergence that extends beyond descriptive or parallel observations, enabling radiation-induced cellular adaptation to be captured as a quantifiable, label-free biophysical phenotype at single-cell resolution. This integrated cytoscopic mechanomics framework enables systematic interrogation of tumor heterogeneity and mechanotype-driven phenotypic plasticity in preclinical models. Beyond advancing fundamental mechanobiological understanding, the platform provides a scalable analytical basis for single-cell–resolved drug screening and mechanobiology-informed therapeutic stratification grounded in quantifiable nanomechanical responses. Furthermore, the mechanotype paradigm defined here provides a foundation for future translational studies evaluating how nanomechanical phenotypes and their associated molecular effectors relate to therapeutic response in human tumors. Although developed at single-cell resolution, this framework is conceptually aligned with emerging AFM-based approaches that assess tumor nanomechanics at the tissue scale, which are being explored as potential diagnostic strategies in cancer research.[88−91] By defining quantifiable mechanophenotypic features at the single-cell level, our approach provides an upstream framework for interpreting tumor mechanical heterogeneity observed at the tissue scale.

Future studies will prioritize IRB-approved validation of this mechanotype framework in patient-derived specimens and advanced ex vivo models to systematically assess its translational relevance in therapeutic response evaluation. These efforts will further clarify how single-cell–resolved mechano-phenotypes interface with tissue-scale mechanical heterogeneity across progressively complex biological systems.

EXPERIMENTAL SECTION

Cell Culture

Human breast cancer cell line (MDA-MB-231) was obtained from KCLB (Korean Cell Line Bank, Seoul, Korea) and cultured with RPMI1640 media (11874−119, Gibco, Carlsbad, CA, USA) supplemented with 10% Fetal Bovine Serum (FBS; 10082−147, Gibco) and 1% Antibiotic-Antimycotic (AA; 15240−062, Gibco) in a humidified incubator containing 5% CO_2 at 37 °C.

Antibodies and Inhibitors

Primary antibodies: Paxillin (ab32084), Rac-1 (ab33186), MT1-MMP (ab51074), Vinculin (ab18058), Cortactin (ab81208) and β-tubulin (ab15568) were acquired from Abcam (Cambridge, MA, USA). Vimentin (5741) was purchased from Cell Signaling Technology (Beverly, MA, USA) and p-34Arc/ARPC2 (07−227) was acquired from Millipore Sigma (Burlington, MA, USA). β-actin (sc-47724) were acquired from Santa Cruz Biotechnology (Dallas, TX, USA) and F-actin (Actin-stain 555 phalloidin; PHDH1) was purchased from Cytoskeleton, Inc. (Denver, CO, USA).

Secondary antibodies: Goat Anti-Rabbit/Mouse IgG H&L (Alexa Fluor488) (ab150077/ab150113) and Donkey Anti-Rabbit/Mouse IgG H&L (Alexa Fluor555, ab150074/ab150106) were purchased from Abcam. The HRP-conjugated antirabbit IgG or antimouse IgG secondary antibodies used for immunoblotting analysis were from Cell signaling Technology. Abberior STAR 488 and Abberior STAR RED (Abberior GmbH, Göttingen, Germany) were used for STED imaging.

X-ray Irradiation Experiments

MDA-MB-231 cells (0.75×10^5 cells/well) were seeded on a 24 well plate. After 24h, the cells were irradiated with different radiation dosages (0, 1, 2, 4, 8, and 10 Gy) using X-RAD 320 X-ray irradiator (Precision X-ray Irradiation, North Branford, CT, USA).

Cell Viability Evaluation by Colony Formation Assay

MDA-MB-231 cells (0.5×10^5 or 1×10^5 cells/well) were plated on a 24 well plate. After 24 h, the cells were exposed to X-ray and incubated 4 days after irradiation. The cells were fixed with 4% paraformaldehyde (P2031, Biosesang, Seongnam, Korea) for 15 min and stained with 1% crystal violet solution-0.25% methanol in distilled H_2O (V5265, Sigma-Aldrich, St. Louis, MO, USA) for 10 min at RT. The CV dye was discarded and washed four times with DPBS and dried. One mL of 95% ethanol was then added to well to solubilize the bound CV dye, and 100 μL of the solution was transferred to a 96-well plate for quantification at an absorbance of 590 nm with Cytation 1 cell imaging multimode reader (Bio-Tek, Winooski, VT, USA). Data were shown as mean average ± standard deviation (n = 4).

Immunofluorescence Staining for Confocal Microscopic Imaging and STED Imaging

MDA-MB-231 cells (0.75×10^5 cells/well) were seeded on round-shape glass coverslips in 24-well plate. After 24 h incubation, the cells were exposed to different radiation dosages (0, 1, 2, 4, 8, and 10 Gy). After 4 days, the cells were fixed for 30 min with 4% paraformaldehyde (PFA; Biosesang, Korea) and washed three times with 1X PBS (Welgene Inc., Korea). For permeabilization, 0.05% Triton X-100 (T9285, Sigma-Aldrich) was treated to cells for 15 min and blocked with 1% bovine serum albumin (BSA; BSAS-NZ, Bovogen, VIC, Australia) and 0.001% sodium azide (26628−22−8, JUNSEI chemical, Tokyo, Japan). The cells were stained with primary antibodies (1:200) and secondary antibodies (1:500). Hoechst33342 (ThermoFisher Scientific) was added for nucleus staining at a final concentration of 5 mg/mL. The confocal microscopic images were captured by LSM700 (Carl Zeiss, Jena, Germany), and the ZEN software was used for analysis. For super-resolution STED imaging, cell images were acquired by a STEDYCON (Abberior Instruments

https://doi.org/10.1021/acsnano.6c04639
ACS Nano XXXX, XXX, XXX−XXX

GmbH, Göttingen, Germany) mounted at the camera port of IX83 inverted microscope (Olympus, Tokyo, Japan) equipped with a 100x objective lens (UPLSAPO100XO/1.4, WD 0.13). The STEDYCON consisted of three excitation wavelengths lasers at 450, 594, and 640 nm and one pulsed STED laser at 775 nm. The skeletal network analysis toolkit was constructed for analyzing the intracellular network of the vimentin and actin filament by Fiji software (http://fiji.sc/; GitHub, San Francisco, CA, USA).

Western Blotting

Total protein was extracted using 1X RIPA buffer (10X; 9806, Cell Signaling) supplemented with 1 mM PMSF (200 mM; 8553, Cell Signaling) and 1X Protease/Phosphatase Inhibitor Cocktail (100X; 5872, Cell Signaling). Protein concentration was determined by the Pierce BCA Protein Assay Kit (23227, ThermoFisher Scientific) according to the manufacturer's instructions. Proteins were separated by 8% to 12% SDS-PAGE gel (S2002, Biosesang) and transferred to an Immobilon-P PVDF membrane (IPVH00010, Millipore, Bedford, MA, USA) using standard techniques. Each membrane was blocked with 5% Non-Fat Powdered Milk (N1059, Biosesang) in 1X TBST (10X; T2006, Biosesang) and incubated with the primary and HRP-linked secondary antibodies. The signals were detected with Immobilon Western Chemiluminescent HRP Substrate (WBKLS0500, Millipore) and Blots were exposed in ImageQuant LAS-4000 mini (GE Healthcare Life Sciences, Pittsburgh, PA, USA).

Nanomechanical Single-Cell Profiling

MDA-MB-231 cells (5×10^5 cells/dish) were seeded into WillCo-dish Glass Bottom dish, Series GWST-5040 (WillCo Wells B.V., Amsterdam, NL), in RPMI1640 supplemented with 10% FBS and 1% AA. The cells were grown for 4 days after X-ray irradiation. The medium was exchanged against HEPES-buffer (Gibco) before the cytoscoping measurement. Atomic force microscopy was performed at room temperature in PeakForce QNM in Fluid mode using a BioScope Resolve AFM (Bruker Nano Surfaces, Santa Barbara, CA, USA) system mounted on an AXIO observer A1 inverted optical microscope (Carl Zeiss, Germany). PeakForce QNM Live Cell Probe A, Calibrated prove (PFQNM-LC-A-CAL; Bruker AFM Probes, Camarillo, CA, USA) (Spring constant: 0.1 N/m, Tip length 18 μm, Tip radius 70 nm, Tip half angle 18°) was used to image the cell surface. The Young's modulus for conical indenter was computed from the slope of the linearized Sneddon equation:

$$(F)^{1/2} = \left(\frac{2}{\pi}\frac{E}{(1-\upsilon^2)}\tan\tan(\alpha)\right)^{1/2}\delta$$

Where F is the force acting on the cantilever tip (from force curve); δ is the indentation depth; υ is the Poisson's ratio (sample dependent, typically 0.2−0.5); α is the half an gle of the indenter; E is Young's modulus (calculated parameter). The 3D Height, PeakForce Error, Ramp, and Modulus signals were used to display the cell surface profiles using Nanoscope Analysis v1.60 (Bruker Nano Surfaces, Santa Barbara, CA, USA). The heat map and histogram graph of cortical stiffness were displayed using Sigmaplot program (Systat Software, Inc.)

Tumor Xenograft Model

Female Balb/c nude mice (5 weeks old) were subcutaneously injected with MDA-MB-231 cells (5×10^6 in 150 μL PBS, n = 5) using a 31-gauge syringe. Four weeks after tumor inoculation, mice were subjected to a single dose of 8 Gy radiation. Tumors were excised, fixed in 10% neutral buffered formalin (HT501320, Sigma-Aldrich), and embedded in paraffin. All animal experiments were performed following the protocols evaluated and approved by the Institutional Animal Care and Use Committee (IACUC) of Yonsei University (Approval Number: 2022−0163).

Histology and Immunohistochemistry

Paraffin-embedded sections (4 μm) were stained with hematoxylin and eosin (H&E) for morphological evaluation. For immunohistochemistry (IHC), antigen retrieval was performed in citrate buffer (ab64214, Abcam) at 121 °C for 15 min, followed by peroxidase blocking with 3% H_2O_2. Sections were incubated with primary antibodies against MT1-MMP (1:100, rabbit mAb, ab51074, Abcam), Pan-cytokeratin (1:250, mouse mAb, ab7753, Abcam), and K_i-67 (1:200, rabbit mAb, ab16667, Abcam). Detection was performed using VECTASTAIN ABC kits (Vector PK6101 for rabbit, PK6102 for mouse, Vector Laboratories, Inc., Newark, CA, USA) and developed with DAB substrate (20 μL stock/1 mL buffer; Vector). Counterstaining was carried out with hematoxylin (H3404, Vector).

Imaging and Analysis

Slides were scanned using a Leica DMI6000B microscope at 20X and 40× magnifications with tile scanning (330 fields/section). Image analysis, including quantification of IHC-DAB staining, was conducted using QuPath software (v0.6.0).[92] For K_i-67 and Pan-cytokeratin, strict thresholds were applied to define intensity categories as negative (<0.15), weak (0.15−0.30), moderate (0.30−0.60), and strong (>0.60). For MT1-MMP, thresholds were adjusted based on its distribution (negative <0.05, weak 0.05−0.12, moderate 0.12−0.20, strong ≥ 0.20) to ensure adequate separation into 1+/2+/3+ categories. Negative cells (class 0) were excluded from comparative distribution

Statistical Analysis

Statistical analyses were performed using GraphPad Prism (version 9). Normality of the data sets was assessed prior to parametric testing. Data are presented as mean ± SD. Statistical significance for group comparisons was determined using one-way ANOVA followed by Tukey's multiple comparison test (*p < 0.05, **p < 0.01, ***p < 0.001). For AFM-based single-cell modulus measurements, statistical differences were evaluated using the Kruskal−Wallis test followed by Dunn's multiple comparison test (***p < 0.001).

■ ASSOCIATED CONTENT

Supporting Information

The Supporting Information is available free of charge at https://pubs.acs.org/doi/10.1021/acsnano.6c04639.

(Notes S1−S14) Schematic illustration and phase-contrast imaging for the investigation of the biomechanical properties of radiation-induced polyploid giant cancer cells (PGCCs); cytoskeletal network analysis of F-actin using skeletonization and z-stack reconstruction; dose-dependent confocal and STED imaging of ARPC2, β-tubulin, Vimentin, Paxillin, Rac-1, and cortactin colocalization; quantitative Cytoskeletal Network Metrics (CNM) for actin and intermediate filament networks; AFM force-volume mapping of energy dissipation and nanoscale surface topography; correlation-based Cyto-Mechanotype Distance Matrix (CMDM) analysis of cyto-mechanical parameters highlighting cortical stiffness relationships; and quantitative classification of immunohistochemical staining intensity for Pan-cytokeratin and K_i-67 in irradiated and non-irradiated tumor tissues (PDF)

■ AUTHOR INFORMATION

Corresponding Authors

Minhee Ku − *Department of Radiology, Yonsei University College of Medicine, Seoul 03722, Republic of Korea; Convergence Research Center for Systems Molecular Radiological Science, Yonsei University, Seoul 03722, Republic of Korea;* orcid.org/0000-0002-1674-1474; Email: imechbio@yonsei.ac.kr

Jaemoon Yang − *Department of Radiology, Yonsei University College of Medicine, Seoul 03722, Republic of Korea;*

https://doi.org/10.1021/acsnano.6c04639
ACS Nano XXXX, XXX, XXX−XXX

Convergence Research Center for Systems Molecular Radiological Science, Yonsei University, Seoul 03722, Republic of Korea; Email: 177hum@yuhs.ac

Authors

Nara Yoon − *Department of Radiology, Yonsei University College of Medicine, Seoul 03722, Republic of Korea*

Jin Sung Kim − *Department of Radiation Oncology, Yonsei Cancer Center, Heavy Ion Therapy Research Institute, Yonsei University College of Medicine, Seoul 03722, Republic of Korea*

Woong Sub Koom − *Department of Radiation Oncology, Yonsei Cancer Center, Heavy Ion Therapy Research Institute, Yonsei University College of Medicine, Seoul 03722, Republic of Korea*

Complete contact information is available at: https://pubs.acs.org/10.1021/acsnano.6c04639

Author Contributions

The manuscript was written through contributions of all authors. All authors have given approval to the final version of the manuscript.

Notes

The authors declare no competing financial interest.

■ ACKNOWLEDGMENTS

This work was financially supported by the National R&D Program through the National Research Foundation of Korea (NRF) grant funded by the Ministry of Science and ICT (NRF- 2020R1A2C1101616, NRF-2021R1A2C1009894, and RS-2024-00440151)

■ ABBREVIATIONS

PGCCs,polyploid giant cancer cells; STED,stimulated emission depletion; TNBC,triple-negative breast cancer; MT1-MMP,membrane-type 1 matrix metalloproteinase; AFM,atomic force microscopy; F-actin,filamentous actin; CNM,Cytoskeletal Network Metrics; NPF,nucleation-promoting factor; ECM,extracellular matrix; FA,focal adhesion; EMT,epithelial-to-mesenchymal transition; MTOC,microtubule-organizing center; MMPs,matrix metalloproteinases; QNM,quantitative nanomechanical; FV,force-volume; CMDM,Cyto-Mechano-type Distance Matrix

■ REFERENCES

(1) Zhang, S.; Mercado-Uribe, I.; Xing, Z.; Sun, B.; Kuang, J.; Liu, J. Generation of cancer stem-like cells through the formation of polyploid giant cancer cells. *Oncogene* **2014**, *33*, 116−128.

(2) Fei, F.; Liu, K.; Li, C.; Du, J.; Wei, Z.; Li, B.; Li, Y.; Zhang, Y.; Zhang, S. Molecular mechanisms by which S100A4 regulates the migration and invasion of PGCCs with their daughter cells in human colorectal cancer. *Front. Oncol.* **2020**, *10*, 182.

(3) Huang, R. X.; Zhou, P. K. DNA damage response signaling pathways and targets for radiotherapy sensitization in cancer. *Signal Transduct. Target. Ther.* **2020**, *5*, 60.

(4) Jiao, Y.; et al. Dormant cancer cells and polyploid giant cancer cells: The roots of cancer recurrence and metastasis. *Clin. Transl. Med.* **2024**, *14*, No. e1567.

(5) Fei, F.; Zhang, M.; Li, B.; Zhao, L.; Wang, H.; Liu, L.; Li, Y.; Ding, P.; Gu, Y.; Zhang, X.; Jiang, T.; Zhu, S.; Zhang, S.; et al. Formation of polyploid giant cancer cells involves in the prognostic value of neoadjuvant chemoradiation in locally advanced rectal cancer. *J. Oncol.* **2019**, *2019*, No. 2316436.

(6) Zhang, Z.; et al. Irradiation-induced polyploid giant cancer cells are involved in tumor cell repopulation via neosis. *Mol. Oncol.* **2021**, *15*, 2219−2234.

(7) Buss, J. H.; Begnini, K. R.; Lenz, G. The contribution of asymmetric cell division to phenotypic heterogeneity in cancer. *J. Cell Sci.* **2024**, *137*, No. jcs261400.

(8) Song, Y.; et al. Stress-induced polyploid giant cancer cells: Unique way of formation and non-negligible characteristics. *Front. Oncol.* **2021**, *11*, No. 724781.

(9) Francescangeli, F.; De Angelis, M. L.; Rossi, R.; Cuccu, A.; Giuliani, A.; De Maria, R.; Zeuner, A.; et al. Dormancy, stemness, and therapy resistance: Interconnected players in cancer evolution. *Cancer Metastasis Rev.* **2023**, *42*, 197−215.

(10) Nyberg, K. D.; et al. Predicting cancer cell invasion by single-cell physical phenotyping. *Integr. Biol. (Camb.)* **2018**, *10*, 218−231.

(11) Zhao, Y.; et al. Physical cytometry: Detecting mass-related properties of single cells. *ACS Sens.* **2022**, *7*, 21−36.

(12) Zhang, S. X.; Liu, L.; Zhao, W. Targeting biophysical cues: A niche approach to study, diagnose, and treat cancer. *Trends Cancer* **2018**, *4*, 268−271.

(13) Ku, M.; et al. Microsphere-based nanoindentation for the monitoring of cellular cortical stiffness regulated by MT1-MMP. *Small* **2018**, *14*, No. e1803000.

(14) Putra, V. D. L.; Kilian, K. A.; Knothe Tate, M. L. Biomechanical, biophysical and biochemical modulators of cytoskeletal remodelling and emergent stem cell lineage commitment. *Commun. Biol.* **2023**, *6*, 75.

(15) DeWane, G.; Salvi, A. M.; DeMali, K. A. Fueling the cytoskeleton − links between cell metabolism and actin remodeling. *J. Cell Sci.* **2021**, *134*, No. jcs248385.

(16) Xuan, B.; et al. Dysregulation in actin cytoskeletal organization drives increased stiffness and migratory persistence in polyploidal giant cancer cells. *Sci. Rep.* **2018**, *8*, 11935.

(17) Yeoman, B.; et al. Adhesion strength and contractility enable metastatic cells to become adurotactic. *Cell Rep.* **2021**, *34*, No. 108816.

(18) Sikic, L.; Schulman, E.; Kosklin, A.; Saraswathibhatla, A.; Chaudhuri, O.; Pokki, J. Nanoscale tracking combined with cell-scale microrheology reveals stepwise increases in force generated by cancer cell protrusions. *Nano Lett.* **2022**, *22*, 7742−7750.

(19) Deville, S. S.; Cordes, N. The extracellular, cellular, and nuclear stiffness, a trinity in the cancer resistome − A review. *Front. Oncol.* **2019**, *9*, 1376.

(20) Petrini, S.; et al. Super-resolution microscopy reveals glioma cell footprints and exosome deposits. *Cell. Adh. Migr.* **2025**, *19*, No. 2534759.

(21) Yuan, J.; et al. ROCK inhibitor enhances mitochondrial transfer via tunneling nanotubes in retinal pigment epithelium. *Theranostics* **2024**, *14*, 5762−5777.

(22) Wu, Z.; Xu, X.; Xi, P. Stimulated emission depletion microscopy for biological imaging in four dimensions: A review. *Microsc. Res. Technol.* **2021**, *84*, 1947−1958.

(23) Jovanović, B.; et al. Heterogeneity and transcriptional drivers of triple-negative breast cancer. *Cell Rep.* **2023**, *42*, No. 113564.

(24) Marra, A.; et al. Practical classification of triple-negative breast cancer: Intratumoral heterogeneity, mechanisms of drug resistance, and novel therapies. *NPJ. Breast Cancer* **2020**, *6*, 54.

(25) Shiao, S. L.; Gouin, K. H.; Ing, N.; Ho, A.; Basho, R.; Shah, A.; Mebane, R. H.; Zitser, D.; Martinez, A.; Mevises, N. Y.; Ben-Cheikh, B.; Henson, R.; Mita, M.; McAndrew, P.; Karlan, S.; Giuliano, A.; Chung, A.; Amersi, F.; Dang, C.; Richardson, H.; Shon, W.; Dadmanesh, F.; Burnison, M.; Mirhadi, A.; Zumsteg, Z. S.; Choi, R.; Davis, M.; Lee, J.; Rollins, D.; Martin, C.; Khameneh, N. H.; McArthur, H.; Knott, S. R. V.; et al. Single-cell and spatial profiling identify three response trajectories to pembrolizumab and radiation therapy in triple-negative breast cancer. *Cancer Cell* **2024**, *42*, 70−84.

(26) Chow, R.; et al. Effect of treatment interruptions on overall survival in patients with triple-negative breast cancer. *J. Natl. Cancer Inst.* **2023**, *115*, 1029−1035.

(27) Zhang, Z.; et al. Morphological profiling by high-throughput single-cell biophysical fractometry. *Commun. Biol.* **2023**, *6*, 449.
(28) Fletcher, D. A.; Mullins, R. D. Cell mechanics and the cytoskeleton. *Nature* **2010**, *463*, 485−492.
(29) Ong, M. S.; et al. Cytoskeletal proteins in cancer and intracellular stress: A therapeutic perspective. *Cancers (Basel)* **2020**, *12*, 238.
(30) Padilla-Rodriguez, M.; et al. The actin cytoskeletal architecture of estrogen receptor positive breast cancer cells suppresses invasion. *Nat. Commun.* **2018**, *9*, 2980.
(31) Ku, M.; Yang, J. Intracellular lipophilic network transformation induced by protease-specific endocytosis of fluorescent Au nanoclusters. *Nano Converg.* **2023**, *10*, 26.
(32) Blanchoin, L.; et al. Actin dynamics, architecture, and mechanics in cell motility. *Physiol. Rev.* **2014**, *94*, 235−263.
(33) Innocenti, M. New insights into the formation and the function of lamellipodia and ruffles in mesenchymal cell migration. *Cell Adh. Migr.* **2018**, *12*, 1−416.
(34) Cheng, Z.; et al. ARPC2 promotes breast cancer proliferation and metastasis. *Oncol. Rep.* **2019**, *41*, 3189−3200.
(35) Rotty, J. D.; et al. Profilin-1 serves as a gatekeeper for actin assembly by Arp2/3-dependent and -independent pathways. *Dev. Cell* **2015**, *32*, 54−67.
(36) Funk, J.; et al. A barbed end interference mechanism reveals how capping protein promotes nucleation in branched actin networks. *Nat. Commun.* **2021**, *12*, 5329.
(37) Lappalainen, P.; Kotila, T.; Jégou, A.; Romet-Lemonne, G.; et al. Biochemical and mechanical regulation of actin dynamics. *Nat. Rev. Mol. Cell Biol.* **2022**, *23*, 836−852.
(38) Graybill, P. M.; Davalos, R. V. Cytoskeletal disruption after electroporation and its significance to pulsed electric field therapies. *Cancers (Basel)* **2020**, *12*, 1132.
(39) Bartak, M.; et al. Equid alphaherpesvirus 1 modulates actin cytoskeleton and inhibits migration of glioblastoma multiforme cell line A172. *Pathogens* **2022**, *11*, 400.
(40) Mavrakis, M.; Juanes, M. A. The compass to follow: Focal adhesion turnover. *Curr. Opin. Cell Biol.* **2023**, *80*, No. 102152.
(41) Shemesh, T.; et al. Focal adhesions as mechanosensors: A physical mechanism. *Proc. Natl. Acad. Sci. U. S. A.* **2005**, *102*, 12383−12388.
(42) Kanchanawong, P.; Calderwood, D. A. Organization, dynamics and mechanoregulation of integrin-mediated cell−ECM adhesions. *Nat. Rev. Mol. Cell Biol.* **2023**, *24*, 142−161.
(43) Bolte, S.; Cordelières, F. P. A guided tour into subcellular colocalization analysis in light microscopy. *J. Microsc.* **2006**, *224*, 213−232.
(44) Franek, M.; et al. Nucleolar reorganization upon site-specific double-strand break induction. *J. Histochem. Cytochem.* **2016**, *64*, 669−686.
(45) Sun, Z.; et al. Integrin-mediated mechanotransduction. *J. Cell Biol.* **2016**, *215*, 445−456.
(46) Pasapera, A. M.; et al. Myosin II activity regulates vinculin recruitment to focal adhesions through FAK-mediated paxillin phosphorylation. *J. Cell Biol.* **2010**, *188*, 877−890.
(47) Yano, H.; et al. Roles played by a subset of integrin signaling molecules in cadherin-based cell−cell adhesion. *J. Cell Biol.* **2004**, *166*, 283−295.
(48) Alpha, K. M.; et al. Paxillin family of focal adhesion adaptor proteins and regulation of cancer cell invasion. *Int. Rev. Cell Mol. Biol.* **2020**, *355*, 1−52.
(49) Deakin, N. O.; Ballestrem, C.; Turner, C. E. Paxillin and Hic-5 interaction with vinculin is differentially regulated by Rac1 and RhoA. *PLoS One* **2012**, *7*, No. e37990.
(50) Xu, J.; et al. Rac1 promotes cell motility by controlling cell mechanics in human glioblastoma. *Cancers (Basel)* **2020**, *12*, 1667.
(51) Gandhi, P. N.; et al. An activating mutant of Rac1 that fails to interact with Rho GDP-dissociation inhibitor stimulates membrane ruffling in mammalian cells. *Biochem. J.* **2004**, *378*, 409−419.
(52) Navarro-Lérida, I.; et al. Rac1 nucleocytoplasmic shuttling drives nuclear shape changes and tumor invasion. *Dev. Cell* **2015**, *32*, 318−334.
(53) Mehidi, A.; Rossier, O.; Schaks, M.; Chazeau, A.; Binamé, F.; Remorino, A.; Coppey, M.; Karatas, Z.; Sibarita, J. B.; Rottner, K.; Moreau, V.; Giannone, G.; et al. Transient activations of Rac1 at the lamellipodium tip trigger membrane protrusion. *Curr. Biol.* **2019**, *29*, 2852−2866.
(54) Yang, M.; et al. Voltage-dependent activation of Rac1 by Nav 1.5 channels promotes cell migration. *J. Cell Physiol.* **2020**, *235*, 3950−3972.
(55) Schaedel, L.; et al. Vimentin intermediate filaments stabilize dynamic microtubules by direct interactions. *Nat. Commun.* **2021**, *12*, 3799.
(56) Gan, Z.; Ding, L.; Burckhardt, C. J.; Lowery, J.; Zaritsky, A.; Sitterley, K.; Mota, A.; Costigliola, N.; Starker, C. G.; Voytas, D. F.; Tytell, J.; Goldman, R. D.; Danuser, G.; et al. Vimentin intermediate filaments template microtubule networks to enhance persistence in cell polarity and directed migration. *Cell Syst.* **2016**, *3*, 252−263.
(57) Gudimchuk, N. B.; McIntosh, J. R. Regulation of microtubule dynamics, mechanics and function through the growing tip. *Nat. Rev. Mol. Cell Biol.* **2021**, *22*, 777−795.
(58) Dogterom, M.; Koenderink, G. H. Actin−microtubule crosstalk in cell biology. *Nat. Rev. Mol. Cell Biol.* **2019**, *20*, 38−54.
(59) Meiring, J. C. M.; Shneyer, B. I.; Akhmanova, A. Generation and regulation of microtubule network asymmetry to drive cell polarity. *Curr. Opin. Cell Biol.* **2020**, *62*, 86−95.
(60) Burakov, A. V.; Nadezhdina, E. S. Centering and shifting of centrosomes in cells. *Cells* **2020**, *9*, 1351.
(61) Meiring, J. C. M.; Shneyer, B. I.; Akhmanova, A. Generation and regulation of microtubule network asymmetry to drive cell polarity. *Curr. Opin. Cell Biol.* **2020**, *62*, 86−95.
(62) Lidke, D. S.; Lidke, K. A. Advances in high-resolution imaging—Techniques for three-dimensional imaging of cellular structures. *J. Cell Sci.* **2012**, *125*, 2571−2580.
(63) Ebrahimi, V.; et al. Deep learning enables fast, gentle STED microscopy. *Commun. Biol.* **2023**, *6*, 674.
(64) Helfand, B. T.; et al. Vimentin organization modulates the formation of lamellipodia. *Mol. Biol. Cell* **2011**, *22*, 1274−1289.
(65) Clark, E. S.; et al. Cortactin is an essential regulator of matrix metalloproteinase secretion and extracellular matrix degradation in invadopodia. *Cancer Res.* **2007**, *67*, 4227−4235.
(66) Ito, A.; et al. The subcellular localization and activity of cortactin is regulated by acetylation and interaction with Keap1. *Sci. Signal.* **2015**, *8*, ra120.
(67) Huang, J.; Asawa, T.; Takato, T.; Sakai, R.; et al. Cooperative roles of Fyn and cortactin in cell migration of metastatic murine melanoma. *J. Biol. Chem.* **2003**, *278*, 48367−48376.
(68) Stock, K.; et al. Overexpression and Tyr421-phosphorylation of cortactin is induced by three-dimensional spheroid culturing and contributes to migration and invasion of pancreatic ductal adenocarcinoma cells. *Cancer Cell Int.* **2019**, *19*, 77.
(69) Mezi, S.; et al. Involvement of the Src−cortactin pathway in migration induced by IGF-1 and EGF in human breast cancer cells. *Int. J. Oncol.* **2012**, *41*, 2128−2138.
(70) Clark, E. S.; Weaver, A. M. A new role for cortactin in invadopodia: Regulation of protease secretion. *Eur. J. Cell Biol.* **2008**, *87*, 581−590.
(71) Hey, S.; Linder, S. Matrix metalloproteinases at a glance. *J. Cell Sci.* **2024**, *137*, No. jcs261898.
(72) Artym, V. V.; et al. Dynamic interactions of cortactin and membrane type 1 matrix metalloproteinase at invadopodia: Defining the stages of invadopodia formation and function. *Cancer Res.* **2006**, *66*, 3034−3043.
(73) Győrffy, B. Survival analysis across the entire transcriptome identifies biomarkers with the highest prognostic power in breast cancer. *Comput. Struct. Biotechnol. J.* **2021**, *19*, 4101−4109.
(74) Alibert, C.; Goud, B.; Manneville, J. B. Are cancer cells really softer than normal cells? *Biol. Cell* **2017**, *109*, 167−189.

https://doi.org/10.1021/acsnano.6c04639
ACS Nano XXXX, XXX, XXX−XXX

(75) Kwon, S.; et al. Comparison of cancer cell elasticity by cell type. *J. Cancer* **2020**, *11*, 5403−5412.
(76) Lv, J.; et al. Cell softness regulates tumorigenicity and stemness of cancer cells. *EMBO J.* **2021**, *40*, No. e106123.
(77) Xing, Y.; et al. Nanoscale structural and mechanical analysis of Bacillus anthracis spores inactivated with rapid dry heating. *Appl. Environ. Microbiol.* **2014**, *80*, 1739−1749.
(78) Maghsoudy-Louyeh, S.; Kropf, M.; Tittmann, B. Review of progress in atomic force microscopy. *Open Neuroimaging J.* **2018**, *12*, 86−104.
(79) Olubowale, O. H.; et al. "May the force be with you!" Force-volume mapping with atomic force microscopy. *ACS Omega* **2021**, *6*, 25860−25875.
(80) Yang, Y.; et al. The comparison between force volume and peakforce quantitative nanomechanical mode of atomic force microscope in detecting cell's mechanical properties. *Microsc. Res. Technol.* **2019**, *82*, 1843−1851.
(81) Liu, H.; et al. In situ mechanical characterization of the cell nucleus by atomic force microscopy. *ACS Nano* **2014**, *8*, 3821−3828.
(82) Cui, J. X.; et al. Tailoring mechanical heterogeneity, nanoscale creep deformation and optical properties of nanostructured Zr-based metallic glass. *Rare Met.* **2023**, *42*, 3430−3442.
(83) Stacey, M.; et al. Nanosecond pulsed electric field induced cytoskeleton, nuclear membrane and telomere damage adversely impact cell survival. *Bioelectrochemistry* **2011**, *82*, 131−134.
(84) Dutta, D.; et al. Energy dissipation mapping of cancer cells. *Micron* **2018**, *105*, 24−29.
(85) Van der Meeren, L.; et al. AFM analysis enables differentiation between apoptosis, necroptosis, and ferroptosis in murine cancer cells. *iScience* **2020**, *23*, No. 101816.
(86) Foerster, F.; et al. Targeting the actin cytoskeleton: Selective antitumor action via trapping PKCε. *Cell Death Dis.* **2014**, *5*, No. e1398.
(87) Liu, X.; et al. Actin cytoskeleton vulnerability to disulfide stress mediates disulfidptosis. *Nat. Cell Biol.* **2023**, *25*, 404−414.
(88) Cross, S. E.; et al. Nanomechanical analysis of cells from cancer patients. *Nat. Nanotechnol.* **2007**, *2*, 780−783.
(89) Plodinec, M.; et al. The nanomechanical signature of breast cancer. *Nat. Nanotechnol.* **2012**, *7*, 757−765.
(90) Puebla-Osorio, N.; et al. Enhanced tumor control and survival in preclinical models with adoptive cell therapy preceded by low-dose radiotherapy. *Front. Oncol.* **2024**, *14*, No. 1407143.
(91) Agrawal, A.; Javanmardi, Y.; Watson, S. A.; Serwinski, B.; Djordjevic, B.; Li, W.; Aref, A. R.; Jenkins, R. W.; Moeendarbary, E.; et al. Mechanical signatures in cancer metastasis. *NPJ. Biol. Phys. Mech.* **2025**, *2*, 3.
(92) Bankhead, P.; et al. QuPath: Open source software for digital pathology image analysis. *Sci. Rep.* **2017**, *7*, 16878.

https://doi.org/10.1021/acsnano.6c04639
ACS Nano XXXX, XXX, XXX−XXX

Supporting Information for

Nanomechanical single-cell profiling reveals mechanical dormancy underlying radiation resistance in polyploid giant cancer cells

*Minhee Ku†, ‡, *, Nara Yoon†, Jin Sung Kim⋐, Woong Sub Koom⋐, Jaemoon Yang†, ‡, **

†Department of Radiology, Yonsei University College of Medicine, Seoul 03722, Republic of Korea

‡Convergence Research Center for Systems Molecular Radiological Science, Yonsei University, Seoul 03722, Republic of Korea

⋐Department of Radiation Oncology, Yonsei Cancer Center, Heavy Ion Therapy Research Institute, Yonsei University College of Medicine, Seoul 03722, Republic of Korea

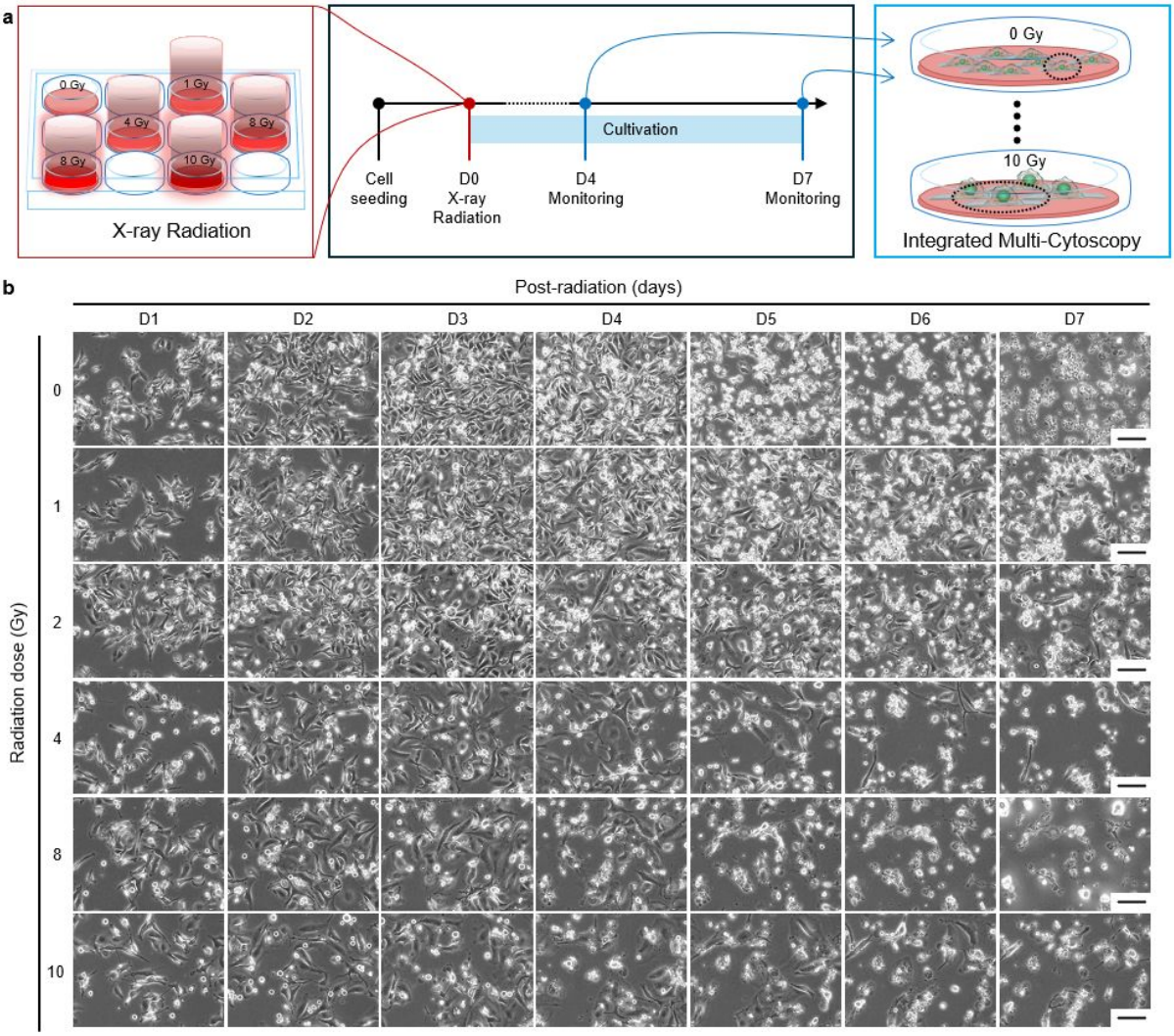

Figure S1. Radiation-induced morphological changes in cancer cells. (a) Schematic illustration of the experimental workflow used to investigate the biomechanical properties of irradiated PGCCs. MDA-MB-231 cells were exposed to X-ray doses of 0, 1, 2, 4, 8, and 10 Gy and cultured for 7 days. (b) Representative phase-contrast microscopy images showing morphological changes following irradiation. Scale bars represent 20 μm.

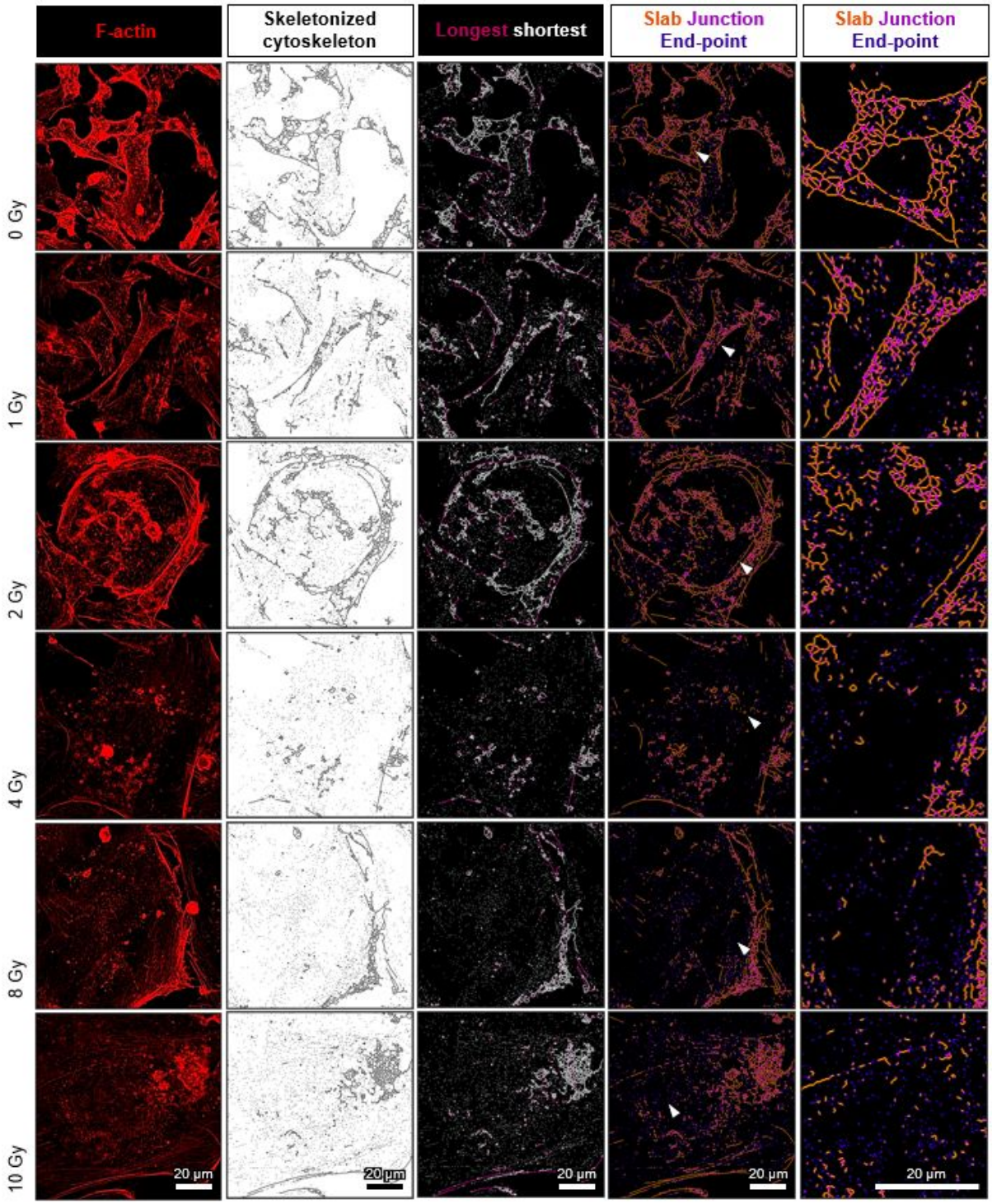

Figure S2. Cytoskeletal network analysis of F-actin distribution in irradiated cancer cells using the skeletonization process. The first column shows confocal microscopy images of irradiated cancer cells stained with phalloidin (red), highlighting the distribution of F-actin. The second column presents the skeletonized cytoskeletal structure. The third column visualizes the longest

and shortest branch paths extracted from the skeletonized network. The fourth column shows the Cytoskeletal Network Metrics (CNM) analysis derived from the skeletonized actin network, including slabs, junctions, and end-points. The fifth column displays magnified views of selected regions indicated by white arrows in the fourth column, highlighting representative structural features of the cytoskeletal network. Scale bars represent 20 μm.

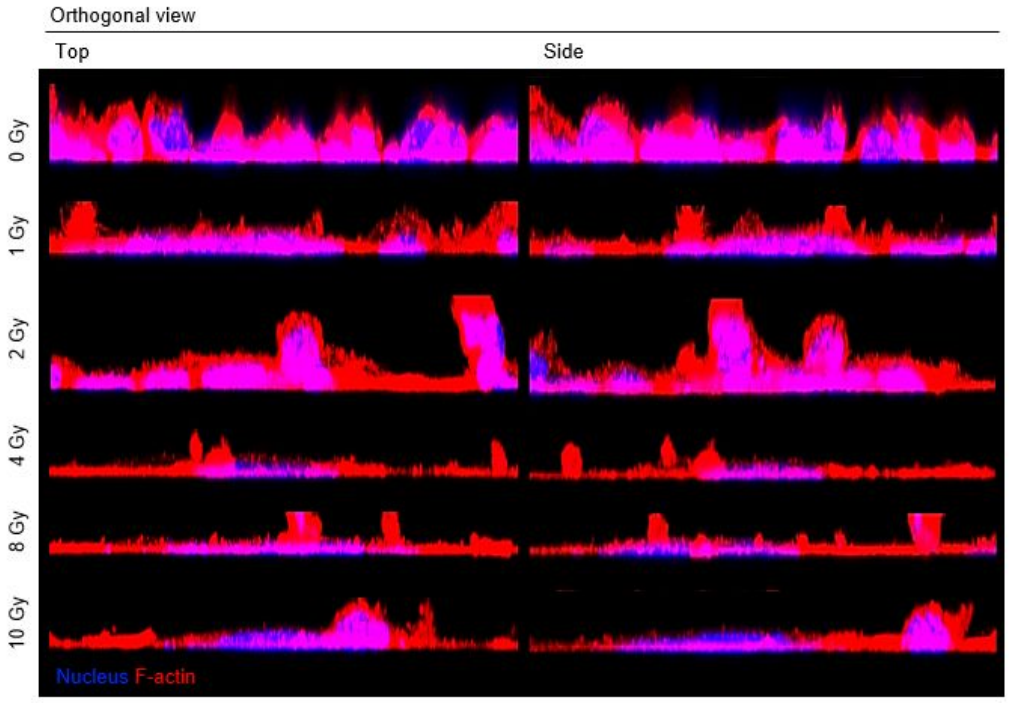

Figure S3. Orthogonal views of the reconstructed cortical F-actin architecture generated from z-stack confocal images are shown in Fig. 2a. The x/z (top) or y/z (side) planes visualize the spatial distribution of F-actin (red) relative to the Nucleus (blue) across increasing radiation doses.

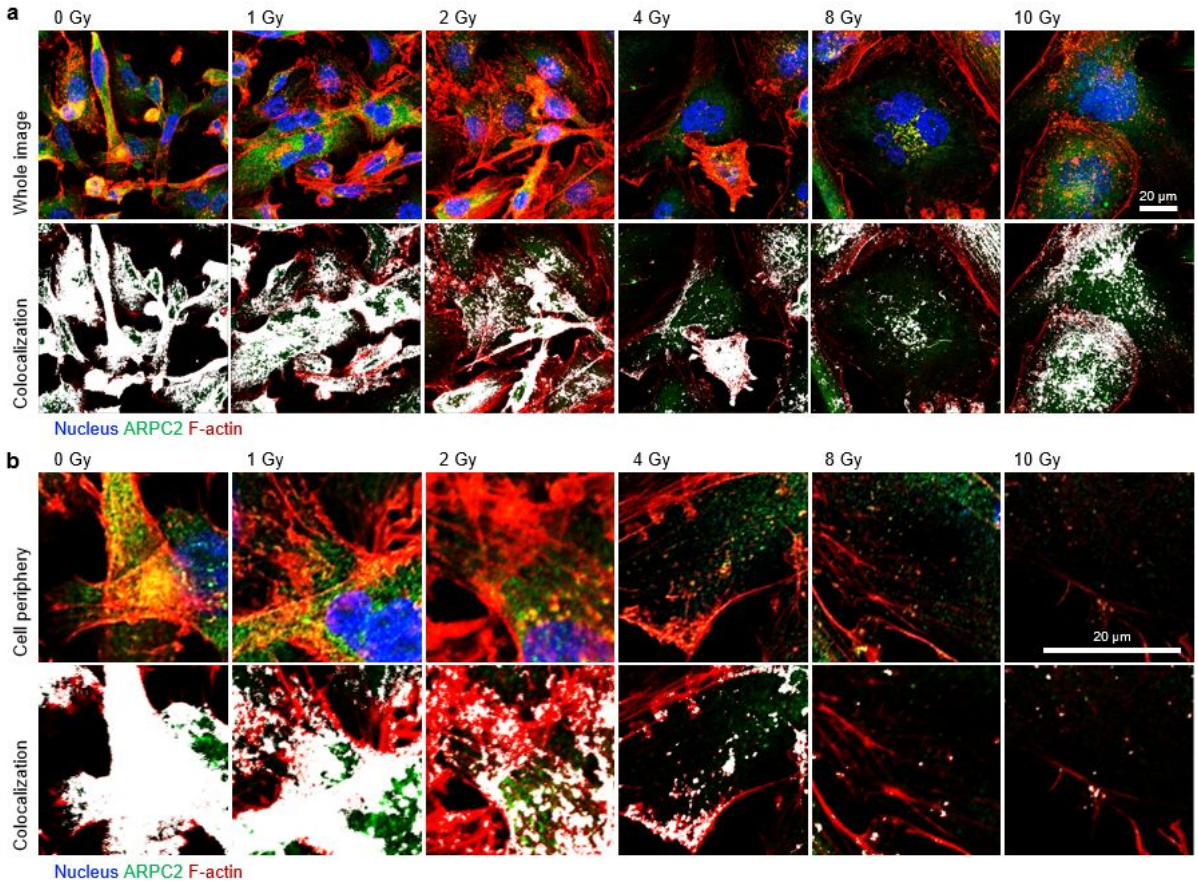

Figure S4. Colocalization analysis of ARPC2 and F-actin in irradiated cancer cells. Representative confocal microscopy images presenting radiation dose-dependent colocalization analysis of ARPC2 (green) and F-actin (red). Nuclei are shown in blue. (a) Whole-cell view displaying ARPC2–actin spatial organization across increasing radiation doses. (b) Magnified views of the cell periphery highlighting colocalization patterns in the cortical region. Scale bars represent 20 μm.

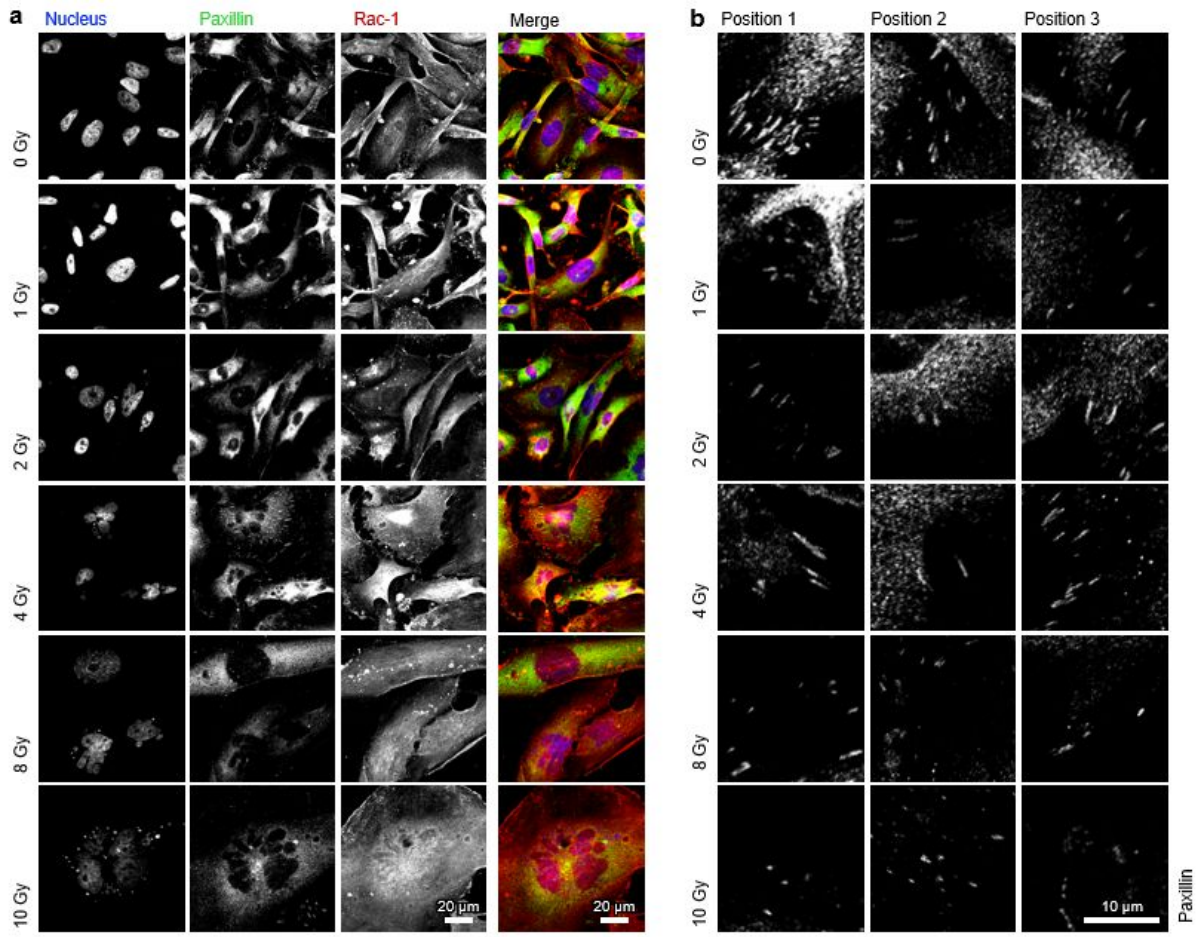

Figure S5. Localization of endogenous Paxillin and Rac1 in irradiated cancer cells. (a) Confocal microscopy images depicting spatial distribution of endogenous Paxillin (green) and Rac-1 (red). Nuclei are shown in blue. Scale bars represent 20 μm. (b) High-magnification images highlighting Paxillin distribution within cell protrusions. Paxillin puncta were segmented and analyzed at three representative protrusion positions. Scale bar represents 10 μm.

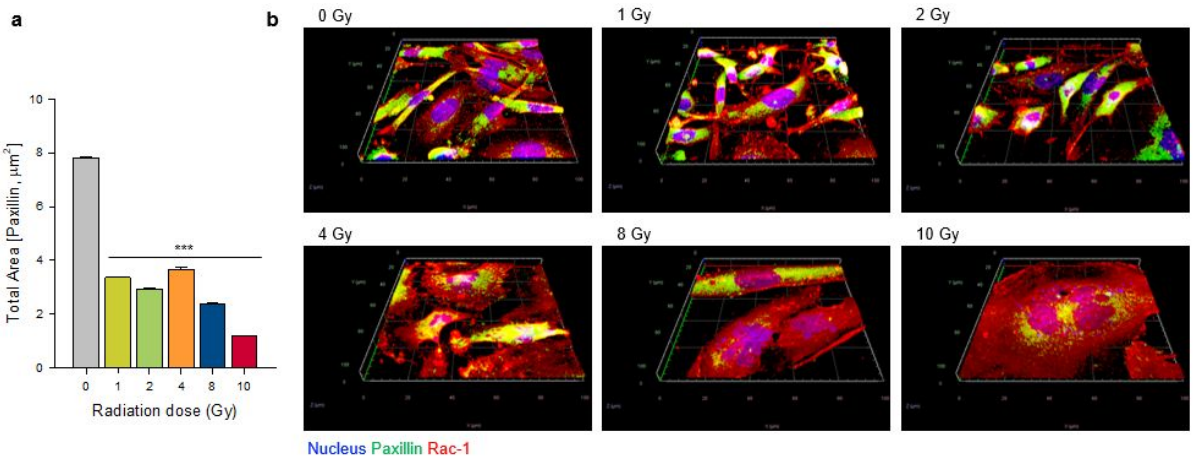

Figure S6. Quantification of Paxillin area and spatial organization. (a) Quantification of total Paxillin area derived from the segmented images shown in Fig. S5b. (b) Three-dimensional surface-rendered reconstructions generated from confocal z-stacks showing the spatial distribution of Paxillin (green) and Rac-1 (red). Nuclei are shown in blue. Data are presented as mean ± SD. Statistical comparisons were performed using one-way ANOVA followed by Tukey's multiple comparison test ($^{*}p < 0.05$, $^{**}p < 0.01$, and $^{***}p < 0.001$)

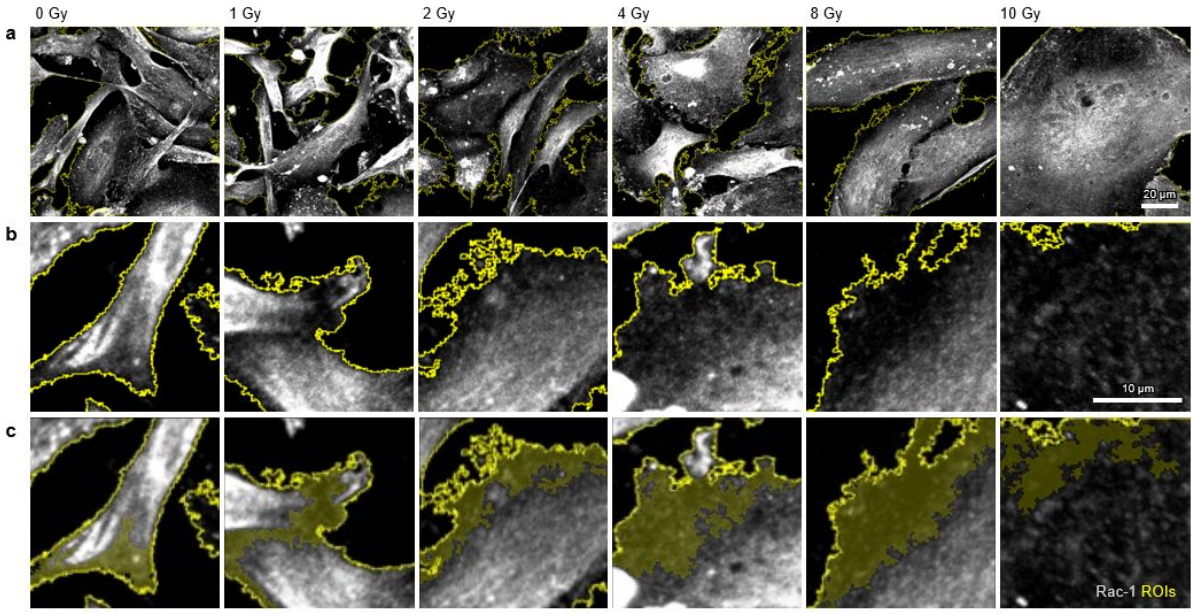

Figure S7. Rac-1 localization and lamellipodial region segmentation. (a) Confocal microscopy images showing Rac-1 distribution within the cytosolic region of irradiated cells. Scale bar represents 20 µm. (b) Magnified image highlighting lamellipodial structures at the cell periphery. Scale bar represents 10 µm. (c) ROI mask highlighting lamellipodial regions used for Rac-1 localization analysis.

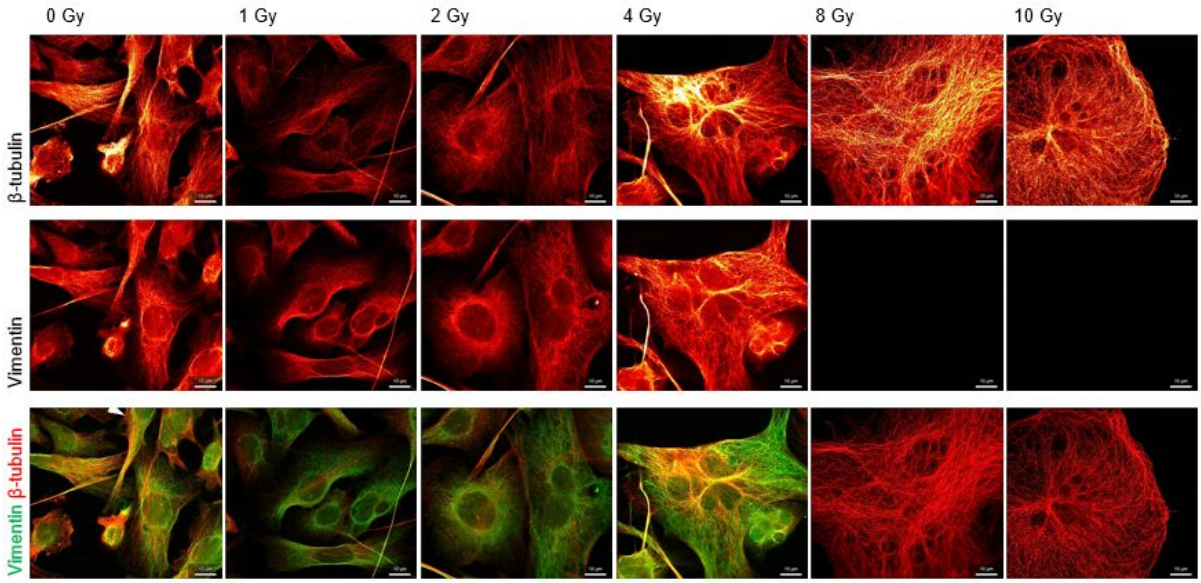

Figure S8. STED microscopy images showing cytoskeletal organization of β-tubulin and vimentin. Representative images illustrate β-tubulin (red) and vimentin (green) distribution across increasing radiation doses (0–10 Gy). Scale bars represent 10 μm.

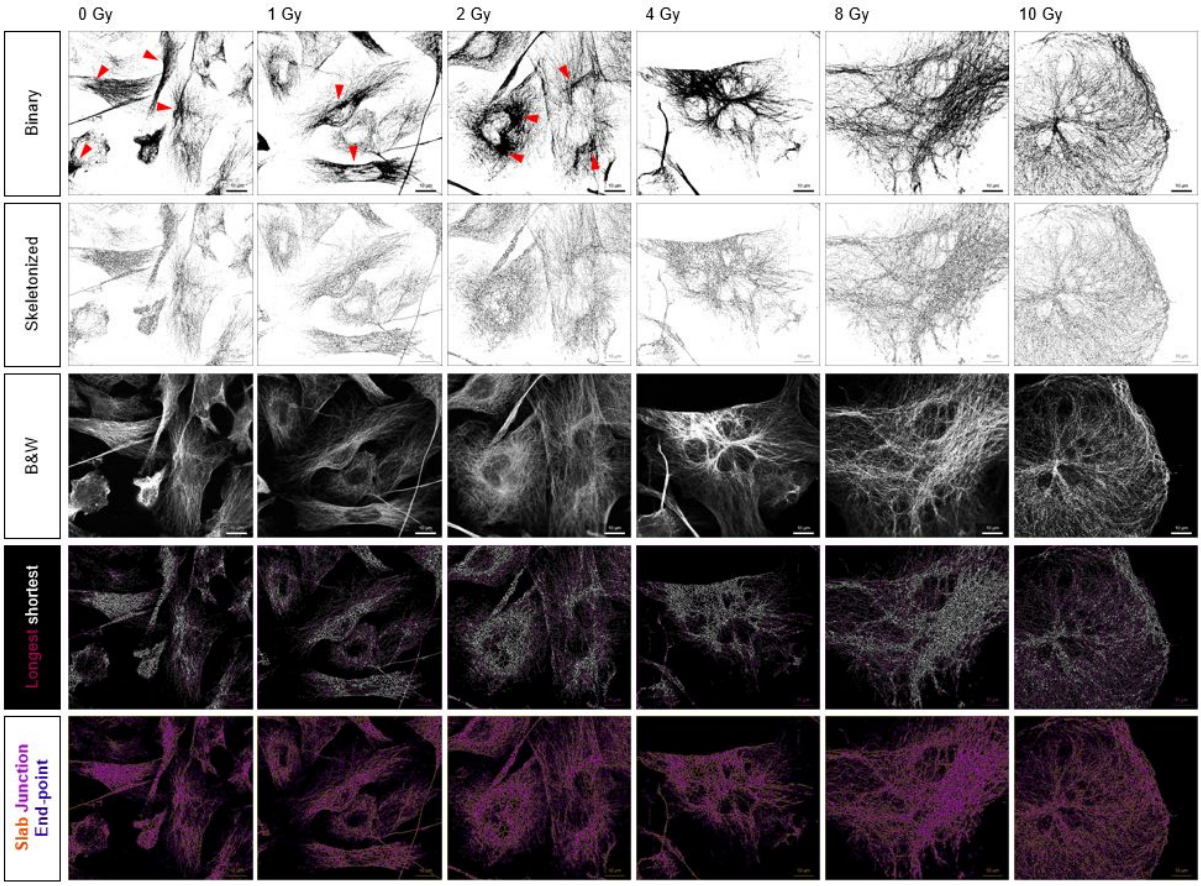

Figure S9. STED-based Cytoskeletal Network Metrics (CNM) analysis of the β-tubulin network. Binary images highlight microtubule organization, with red triangles indicating the microtubule-organizing center (MTOC) based on representative STED microscopy images shown in Fig. S8. Skeletonized representations were used to analyze the architecture of the β-tubulin filament network. The longest (white) and shortest (magenta) paths within the β-tubulin network are shown. Network features were classified based on node connectivity (purple: Junctions, more than 2 neighbors; orange: Slabs, exactly 2 neighbors; blue: End-points, less than 2 neighbors). Scale bars represent 10 μm.

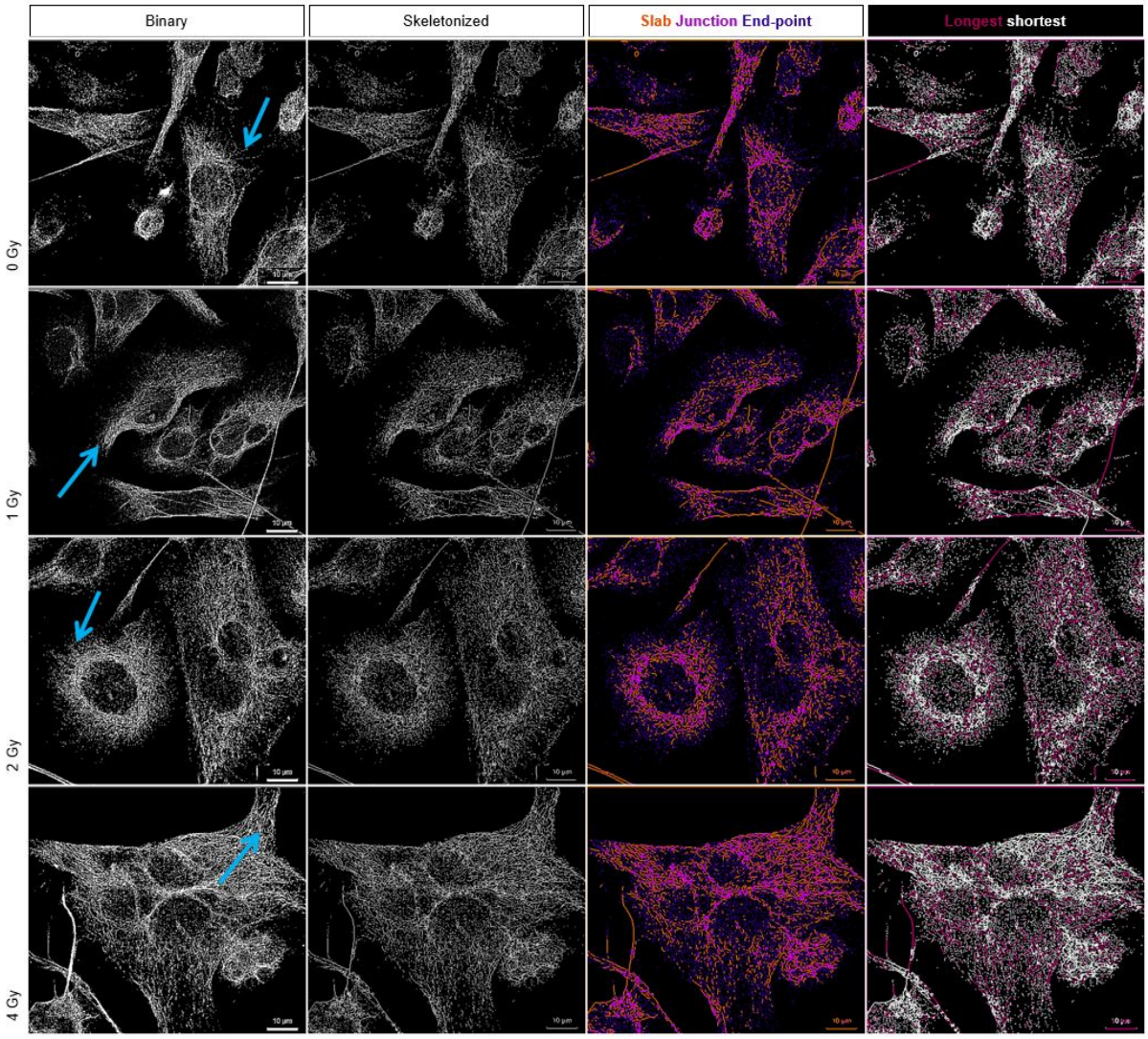

Figure S10. Cytoskeletal Network Metrics (CNM) analysis of the vimentin network. Binary and skeletonized representations were used to analyze the architecture of the vimentin filament network based on representative STED microscopy images shown in Fig. S8. Sky-blue arrows indicate representative cell periphery regions. Network features were classified according to node connectivity (Slabs, Junctions, and End-points), and the longest (white) and shortest (magenta) paths within the network were visualized. Scale bars represent 10 μm.

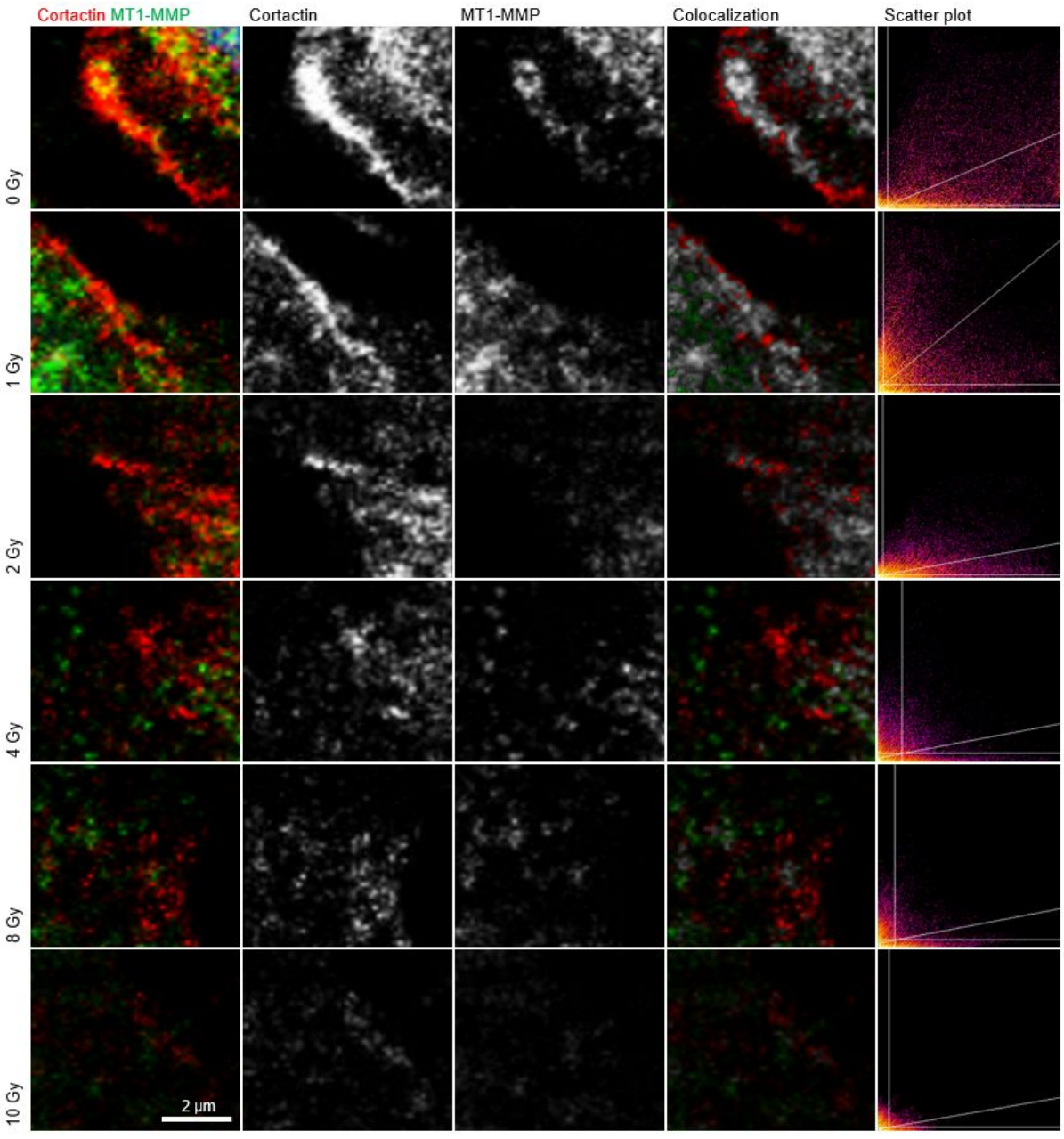

Figure S11. Colocalization analysis of Cortactin and MT1-MMP at membrane protrusion regions. Representative fluorescence images showing Cortactin (red) and MT1-MMP (green) distribution across increasing radiation doses. Individual channels are shown in grayscale, and

overlapping signals are highlighted in the colocalization panels. Pixel-intensity scatter plots display the correlation between Cortactin and MT1-MMP signals in protrusive regions. Scale bar represents 2 μm.

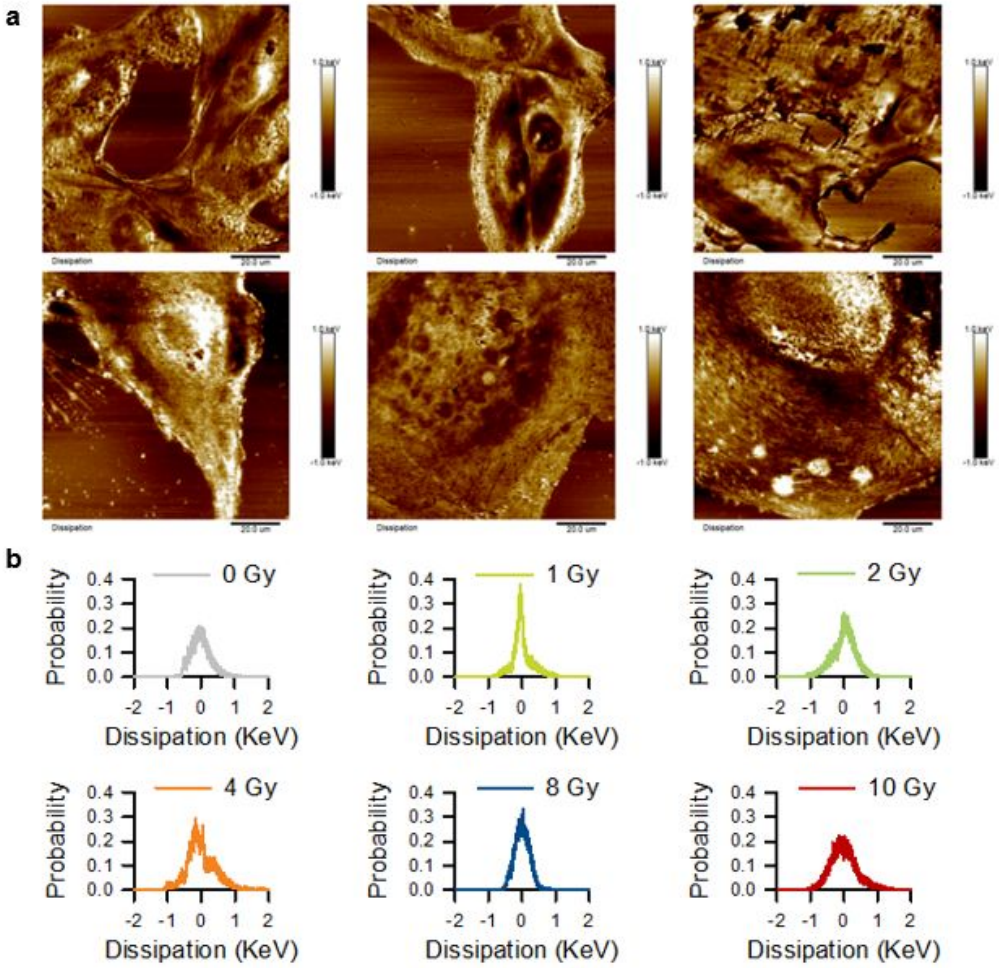

Figure S12. AFM-based energy dissipation analysis using force–volume (FV) mode. (a) Representative energy dissipation maps obtained from AFM force–volume measurements of cells exposed to increasing radiation doses. Scale bars represent 20 μm. (b) Probability distributions of energy dissipation derived from the corresponding AFM force–volume measurements.

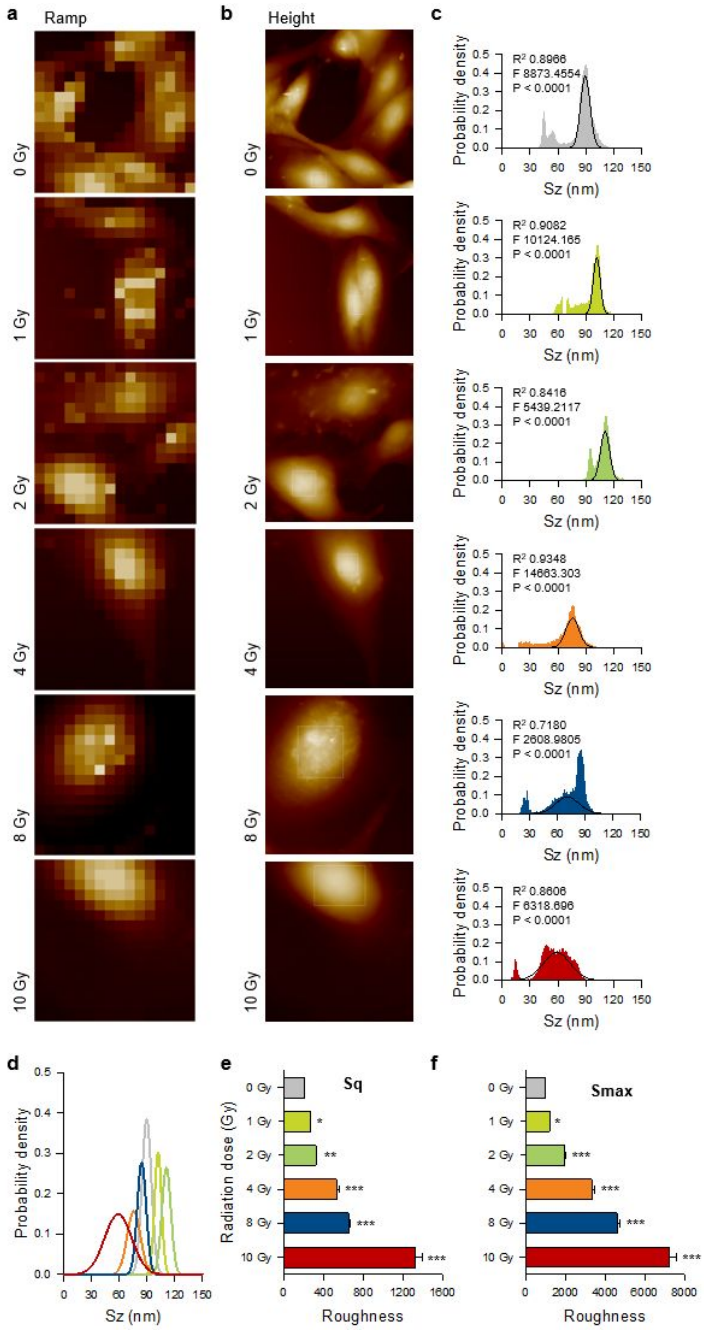

Figure S13. AFM-based surface topography and roughness analysis of cells exposed to increasing radiation doses using force–volume (FV) mode. (a) Representative ramp and (b) corresponding height images obtained from AFM force–volume measurements. (c) Probability density distributions of surface height (Sz) extracted from the regions indicated by yellow rectangles in b. Statistical parameters obtained from regression analysis are indicated as the

coefficient of determination (R^2), F-statistic (F), and P-value (P). (d) Overlays of the probability density distributions shown in c. (e) Quantification of the average root mean square surface roughness (Sq) and (f) the maximum peak-to-valley over the surface (Smax) derived from AFM height images. Data are presented as mean ± SD. Statistical significance was determined using one-way ANOVA followed by Tukey's multiple comparison test (*$p < 0.05$, **$p < 0.01$, ***$p < 0.001$).

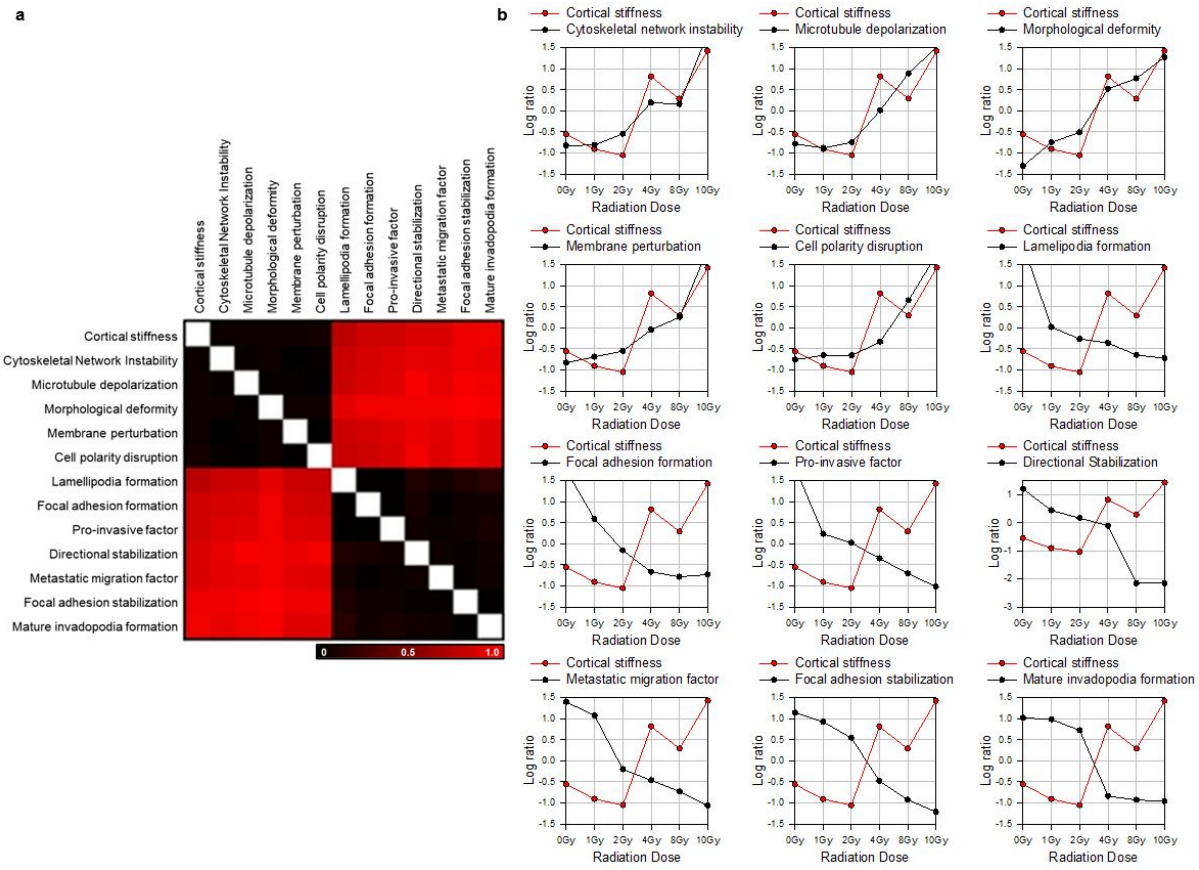

Figure S14. Cyto-Mechanotype Distance Matrix (CMDM) analysis of radiation-dependent cyto-mechanical parameters. (a) Correlation heatmap showing relationships among biomechanical and morphological parameters across radiation doses, generated using MeV software. Each element represents the correlation distance between parameter pairs, ranging from 0 (black, minimal dissimilarity) to 1.0 (red, maximal dissimilarity). (b) Line plots showing radiation-dependent trends of cortical stiffness (red) relative to other cyto-mechanical parameters (black). Values are presented as log ratios relative to the 0 Gy condition.

Table 1. Quantitative assessment of immunohistochemical staining for pan-cytokeratin and Ki-67 in irradiated (RTx) and non-irradiated (Non-RTx) tumor tissues. Staining intensity was quantified using the H-score method $H - score = \sum(Pi \times i)$, where Pi is the percentage of cells at each staining intensity and i denotes staining intensity (0–3).

Marker	Treatment condition	H-score	% Negative	% Positive		
				1+	2+	3+
Pan-cytokeratin	Non-RTx	38.98	70.83	21.24	6.05	1.88
	RTx	32.93	76.13	15.79	7.10	0.98
Ki-67	Non-RTx	20.48	85.71	9.52	3.33	1.43
	RTx	18.50	83.85	14.10	1.76	0.29